NeuroImage 221 (2020) 117154

Contents lists available at ScienceDirect

NeuroImage

journal homepage: www.elsevier.com/locate/neuroimage

PET imaging of neurotransmission using direct parametric reconstruction

Yoann Petibon [a,*], Nathaniel M. Alpert [a], Jinsong Ouyang [a], Diego A. Pizzagalli [b], Cristina Cusin [c], Maurizio Fava [c], Georges El Fakhri [a], Marc D. Normandin [a]

[a] Gordon Center for Medical Imaging, Department of Radiology, Massachusetts General Hospital and Harvard Medical School, Boston, MA, USA
[b] Center for Depression, Anxiety & Stress Research, McLean Hospital and Harvard Medical School, Belmont, MA, USA
[c] Department of Psychiatry, Massachusetts General Hospital and Harvard Medical School, Boston, MA, USA

ARTICLE INFO

Keywords:
PET
Parametric imaging
Direct reconstruction
Neurotransmission
Dopamine

ABSTRACT

Receptor ligand-based dynamic Positron Emission Tomography (PET) permits the measurement of neurotransmitter release in the human brain. For single-scan paradigms, the conventional method of estimating changes in neurotransmitter levels relies on fitting a pharmacokinetic model to activity concentration histories extracted after PET image reconstruction. However, due to the statistical fluctuations of activity concentration data at the voxel scale, parametric images computed using this approach often exhibit low signal-to-noise ratio, impeding characterization of neurotransmitter release. Numerous studies have shown that direct parametric reconstruction (DPR) approaches, which combine image reconstruction and kinetic analysis in a unified framework, can improve the signal-to-noise ratio of parametric mapping. However, there is little experience with DPR in imaging of neurotransmission and the performance of the approach in this application has not been evaluated before in humans. In this report, we present and evaluate a DPR methodology that computes 3-D distributions of ligand transport, binding potential (BP_{ND}) and neurotransmitter release magnitude (γ) from a dynamic sequence of PET sinograms. The technique employs the linear simplified reference region model (LSRRM) of Alpert et al. (2003), which represents an extension of the simplified reference region model that incorporates time-varying binding parameters due to radioligand displacement by release of neurotransmitter. Estimation of parametric images is performed by gradient-based optimization of a Poisson log-likelihood function incorporating LSRRM kinetics and accounting for the effects of head movement, attenuation, detector sensitivity, random and scattered coincidences. A ^{11}C-raclopride simulation study showed that the proposed approach substantially reduces the bias and variance of voxel-wise γ estimates as compared to standard methods. Moreover, simulations showed that detection of release could be made more reliable and/or conducted using a smaller sample size using the proposed DPR estimator. Likewise, images of BP_{ND} computed using DPR had substantially improved bias and variance properties. Application of the method in human subjects was demonstrated using ^{11}C-raclopride dynamic scans and a reward task, confirming the improved quality of the estimated parametric images using the proposed approach.

1. Introduction

Dynamic Positron Emission Tomography (PET) with appropriate neuroreceptor radioligands permits the measurement of neurotransmitter release in the human brain. For instance, PET used in conjunction with ^{11}C-raclopride, a D_2–like receptor antagonist radioligand, can detect transient changes in endogenous striatal dopamine concentration following administration of amphetamine (Breier et al., 1997) or a motor planning task (Alpert et al., 2003). This imaging technique has been used for more than two decades to probe the neurochemical underpinnings of cognitive and motivational functions in normal and neuropathological conditions, including substance abuse (Volkow et al., 1997; Cox et al., 2009; Busto et al., 2009; Martinez et al., 2005), schizophrenia (Breier et al., 1997; Abi-Dargham et al., 1998), Tourette's syndrome (Singer et al., 2002; Wong et al., 2008) and Parkinson's disease (Lidstone et al., 2010; Tedroff et al., 1996; Fuente-Fernández et al., 2001; Steeves et al., 2009).

The competition between radioligand and neurotransmitter for binding to receptor sites is the fundamental principle underpinning the technique. Thus, changes in the synaptic concentration of endogenous

* Corresponding author. 125 Nashua St, Suite 6500, Boston, MA, 02115, USA.
E-mail address: ypetibon@mgh.harvard.edu (Y. Petibon).

https://doi.org/10.1016/j.neuroimage.2020.117154
Received 26 May 2020; Received in revised form 6 July 2020; Accepted 7 July 2020
Available online 15 July 2020

neurotransmitter following a stimulus can perturb the binding kinetics of the radioligand to the receptors, "displacing" the radioligand, and resulting in an effect that can be detected with PET. A variety of experimental designs and data analysis methods have been proposed to measure radioligand displacement. Some approaches require the subject to undergo two dynamic PET scans - one at baseline and the other immediately after stimulation - and estimate neurotransmitter release by measuring changes in radioligand binding (e.g. variation in binding potential) between the two acquisitions (Koepp et al., 1998). This design has the merit of simplicity of analysis because standard methods such as the simplified reference tissue model (Lammertsma and Hume, 1996) can be used to quantify binding in the two conditions. It has limitations, however, including radiation exposure, high costs and the fact that the system may not be at physiological steady state during the second scan (Alpert et al., 2003). Furthermore, the use of two separate scanning sessions introduces a source of experimental error that may reduce the sensitivity of the method. To mitigate these shortcomings, single-scan paradigms have been developed and successfully used to image neurotransmission (Friston et al., 1997; Richard E. Carson et al., 1997; Alpert et al., 2003; Pappata et al., 2002; Normandin et al., 2012). These experimental designs require the stimulus to be performed during scanning and usually involve the use of more advanced, non-steady state pharmacokinetic models designed to capture changes in kinetic parameters (Alpert et al., 2003; Normandin et al., 2012). For completeness, it should be noted that some investigators have developed kinetic analyses methods that not only enable detection of release but also estimation of time-courses of neurotransmitter concentration from PET time-activity curves (TACs) (Constantinescu et al., 2007; Morris et al., 2005). Recently, Lippert and colleagues (Lippert et al., 2019) have proposed and validated a new technique to study dopaminergic activity using PET and a bolus-plus-infusion of ^{11}C-raclopride that does not rely on compartmental modeling, but instead on direct analysis of temporal (i.e. frame-by-frame) variations of ^{11}C-raclopride signal in tissue.

Regardless of the experimental design, the conventional approach to measuring changes in neurotransmitter levels consists in fitting a pharmacokinetic model to reconstructed TACs, typically using least-square regression methods. A limitation of this approach, however, is that it yields parameter estimates with low accuracy and precision when applied at the voxel level. Two factors explain the poor performance of the standard method. First, the TACs of single voxels have a low signal-to-noise-ratio (SNR) and many solutions to the fitting process yield similar sums of squared residuals. Thus, estimates of model parameters have large uncertainties. Second, statistically efficient parameter estimation depends on an accurate modeling of the noise distribution in the data (i.e., TACs) during fitting. However, precise modeling of the noise in the reconstructed PET images is challenging, owing to its space-varying and object-dependent properties (Barrett et al., 1994; Fessler, 1996; Wang and Qi, 2010).

While the low SNR constitutes an impediment to virtually all applications of dynamic PET, it especially hinders voxel-wise analyses of single-scan neurotransmission experiments where the task is to quantify relatively small perturbations in very noisy TACs. A simple and straightforward approach to mitigate the impact of noise is to convolve the dynamic PET volumes with smoothing kernels before model fitting. Although smoothing can drastically reduce noise, it comes at the price of a lower effective resolution and greater partial volume effects in the smoothed images that may in turn reduce the apparent magnitude of displacement and complicate the detection of weaker and more localized effects. In practice, analyses are thus still mostly performed at the regional level using TACs extracted in regions of interest (ROIs) chosen a priori. The implicit assumption is that the selected regions are functionally homogenous; however, release may only occur in a small subset of the voxels in the ROI and averaging across the entire region may thus swamp the signal from these voxels with that from other non-activated voxels, which may reduce the sensitivity of the technique. More generally, ROI analyses involve a tradeoff between using larger regions with better TAC SNR but poorer spatial information, and smaller regions with lower SNR but finer spatial information.

Approaches that estimate parametric images directly from the measured projections (techniques also known as direct parametric reconstruction - 'DPR') have been proposed to increase the SNR of parametric PET (Wang and Qi 2009, 2013, 2010; Kamasak et al., 2005; Yan et al., 2012; Tsoumpas et al., 2008; Rahmim et al., 2009; Reader and Verhaeghe, 2014; Rakvongthai et al., 2013; Petibon et al., 2017; Gravel and Reader, 2015). The SNR improvement afforded by DPR as compared to the standard post-reconstruction estimation approach (or "indirect" parametric reconstruction – 'IPR') is due to two main factors. First, DPR is more efficient than IPR from a statistical standpoint, in the sense that more accurate estimates of noise are available for the projections (Poisson) than are for the reconstructed images and TACs. As a result, the DPR estimator more efficiently compensates noise propagation from the projection measurements to the fitting process and the resulting parametric maps (Wang and Qi, 2013). Second, by combining image reconstruction and kinetic modeling in a unified algorithm, DPR essentially introduces temporal regularization in the reconstruction of dynamic emission data via the kinetic model. Although the basic theory of DPR has been proposed more than 30 years ago (Carson and Lange, 1985; Snyder, 1984), the approach has received renewed interest in the last decade as improvements in computational power have helped overcome the computationally intensive burden of this reconstruction problem (Wang and Qi, 2013). Nevertheless, there is surprisingly little experience with DPR in imaging of neurotransmission: to our knowledge, a single study (Angelis et al., 2018) has investigated the use of DPR together with the linear parametric neurotransmitter PET model (Normandin et al., 2012) using ^{11}C-raclopride and an amphetamine challenge in rat.

Extending our methodological developments in PET mapping of myocardial blood flow (Rakvongthai et al., 2013; Petibon et al., 2017), we present and evaluate a DPR technique designed to increase the SNR of parametric images obtained in single-scan neurotransmission experiments so that neurotransmitter release might be more accurately characterized in individual subjects and cohorts alike. Here, we focused on the detection of release and used the linear simplified reference region model (LSRRM) of Alpert et al., (2003) for modeling the temporal evolution of the distribution of radioligand during the experiment. By analyzing realistic ^{11}C-raclopride simulations, we show that the proposed approach provides more accurate and precise images of neurotransmitter release magnitude and ligand binding potential than the more conventional approach that involves kinetic modeling post reconstruction. We also demonstrate application of the technique to human subjects by analyzing ^{11}C-raclopride data acquired during a monetary reward task (to elicit dopamine release) using a whole-body PET/MR camera.

2. Materials and methods

In what follows, we first present the kinetic model used in this work, then describe the standard and proposed parameter estimators as well as the simulation and experimental studies performed to evaluate the proposed methodology. Note that non-bold letters (e.g. x) represent scalars, bold lower-case letters (e.g. $\mathbf{x}$) represent vectors and bold upper-case letters (e.g. $\mathbf{X}$) represent matrices. IPR = "Indirect Parametric Reconstruction", DPR = "Direct Parametric Reconstruction".

2.1. Kinetic model

The LSRRM analysis technique developed by Alpert et al., (2003) is an extension of the simplified reference tissue model (SRTM, (Lammertsma and Hume, 1996)). There is however a fundamental difference between LSRRM and SRTM: while SRTM assumes a physiological steady state throughout the experiment, LSRRM assumes that the steady state is not maintained and allows the dissociation rate of the radioligand (i.e., rate of radioligand efflux from the collapsed tissue compartment to the plasma - k_{2a}) to change during the scan in response to an altered synaptic

concentration of neurotransmitter. The basic equation describing the instantaneous tissue concentration of radioligand as a function of time is:

$$C_T(t) = R_1 C_R(t) + k_2 \int_0^t C_R(\tau)d\tau - \int_0^t k_{2a}(\tau) C_T(\tau)d\tau \quad (1)$$

where C_T and C_R are concentrations of radioligand in tissue with specific binding and a region devoid of receptors ("reference region"), respectively, R_1 is the ratio of inward transport rates for the binding and reference regions, k_2 describes the clearance of nonspecifically bound radioligand from the tissue to plasma and $k_{2a}(t)$ is a time-varying parameter that includes information about radioligand dissociation from the receptor to plasma. Alpert et al. set $k_{2a}(t) = k_{2a} + \gamma h(t)$ where k_{2a} is the apparent baseline tissue washout rate, $h(t)$ encodes the temporal variation of the dissociation rate due to displacement of radioligand and γ encodes the magnitude of the effect. The binding potential can be computed from the model parameters as $BP_{ND} = k_2/k_{2a} - 1$. The operational equation for LSRRM is given by

$$C_T(t) = R_1 C_R(t) + k_2 \int_0^t C_R(\tau)d\tau - k_{2a} \int_0^t C_T(\tau)d\tau - \gamma \int_0^t C_T(\tau) h(\tau)d\tau \quad (2)$$

Alpert and colleagues assumed that the temporal kinetics of the neurotransmitter response are known a priori, setting:

$$h(t) = e^{-\alpha(t-t_s)} u(t - t_s) \quad (3)$$

where $u(t)$ is the Heaviside step function and t_s is the time at which activation commences. This formulation, used previously by Endres and Carson, (1998) to model dopamine release after administration of amphetamine, assumes a response that becomes maximal instantaneously at the onset of the stimulus and then diminishes exponentially over time with a rate α (min^{-1}). The LSRRM method thus relies on four parameters (R_1, k_2, k_{2a}, γ) to describe the kinetics of radioligand in binding tissue during a neurotransmission experiment. Release of neurotransmitter is detected by testing whether γ is statistically different than zero (Alpert et al., 2003).

2.2. Calculation of parametric images

2.2.1. Standard method: indirect parametric reconstruction

For indirect parametric reconstruction (IPR), the four model parameters are estimated by least-square fitting of LSRRM to the TAC of every voxel, i.e., after reconstruction of the PET scan data (dynamic projections) into a temporal series of images ("frames") and application of motion correction.

Data Model. The expected value of the reconstructed activity concentration in a frame is modeled as the integrated value of the instantaneous concentration of radioligand over the frame duration

$$\bar{x}_T^m = \frac{1}{\Delta_m} \int_{t_m}^{t_m+\Delta_m} C_T(\tau) e^{-\lambda\tau} d\tau \quad (4)$$

$$\bar{x}_R^m = \frac{1}{\Delta_m} \int_{t_m}^{t_m+\Delta_m} C_R(\tau) e^{-\lambda\tau} d\tau \quad (5)$$

where $m \in [1 \ldots M]$ refers to an arbitrary frame with start time t_m and duration Δ_m, $\bar{x}_T^m$ and $\bar{x}_R^m$ denote expected values of activity in tissue with specific binding and the reference region, respectively, and λ (min^{-1}) is the decay constant of the radioisotope. Note that $\bar{x}_T^m$ and $\bar{x}_R^m$ represent non-decay-corrected measures of activity concentration. Time-integration of Eq. (2) over t_m and substitution into Eq. (4) after approximation of the integrals as sums, allows one to express the model-predicted tissue activity concentration as a function of the four model parameters and the reference region TAC:

$$\bar{x}_j^m \approx R_1^j \bar{x}_R^m + k_2^j L_m \left(\sum_{n=1}^{m} \frac{\Delta_n \bar{x}_R^n}{L_n} - \frac{\Delta_m \bar{x}_R^m}{2L_m} \right) - k_{2a}^j L_m \left(\sum_{n=1}^{m} \frac{\Delta_n \bar{x}_j^n}{L_n} - \frac{\Delta_m \bar{x}_j^m}{2L_m} \right) - \gamma^j L_m \left(\sum_{n=1}^{m} \frac{\Delta_n \bar{x}_j^n}{L_n} h\left(t_n + \frac{\Delta_n}{2}\right) - \frac{\Delta_m \bar{x}_j^m}{2L_m} h\left(t_m + \frac{\Delta_m}{2}\right) \right) \quad (6)$$

where j is an index for a binding voxel and $L_m = e^{-\lambda t_m} \frac{1 - e^{-\lambda \Delta_m}}{\lambda \Delta_m}$ accounts for radioactive decay at frame m. Based on Eq. (6), the expected TAC in voxel j noted $\bar{\mathbf{x}}_j = [\bar{x}_j^1 \ldots \bar{x}_j^M]^T \in \mathbb{R}^{M \times 1}$ can be expressed as a function of the vector of parameters $\boldsymbol{\theta}_j = [R_1^j \; k_2^j \; k_{2a}^j \gamma^j]^T \in \mathbb{R}^{4 \times 1}$ through the linear transform $\bar{\mathbf{x}}_j = \mathbf{A}_j \boldsymbol{\theta}_j$, where

$$\mathbf{A}_j = \begin{bmatrix} \bar{x}_1^R & L_1 \left(\sum_{n=1}^{1} \frac{\Delta_n \bar{x}_R^n}{L_n} - \frac{\Delta_1 \bar{x}_R^1}{2L_1} \right) & -L_1 \left(\sum_{n=1}^{1} \frac{\Delta_n \bar{x}_j^n}{L_n} - \frac{\Delta_1 \bar{x}_j^1}{2L_1} \right) & -L_1 \left(\sum_{n=1}^{1} \frac{\Delta_n \bar{x}_j^n h\left(t_n + \frac{\Delta_n}{2}\right)}{L_n} - \frac{\Delta_1 \bar{x}_j^1 h\left(t_1 + \frac{\Delta_1}{2}\right)}{2L_1} \right) \\ \vdots & \vdots & \vdots & \vdots \\ \bar{x}_M^R & L_M \left(\sum_{n=1}^{M} \frac{\Delta_n \bar{x}_R^n}{L_n} - \frac{\Delta_M \bar{x}_R^M}{2L_M} \right) & -L_M \left(\sum_{n=1}^{M} \frac{\Delta_n \bar{x}_j^n}{L_n} - \frac{\Delta_M \bar{x}_j^M}{2L_M} \right) & -L_M \left(\sum_{n=1}^{M} \frac{\Delta_n \bar{x}_j^n h\left(t_n + \frac{\Delta_n}{2}\right)}{L_n} - \frac{\Delta_M \bar{x}_j^M h\left(t_M + \frac{\Delta_M}{2}\right)}{2L_M} \right) \end{bmatrix} \quad (7)$$

with $\mathbf{A}_j \in \mathbb{R}^{M \times 4}$.

Parameter estimation. Under the standard assumption that the temporal activity concentration for any voxel are realizations of normally distributed and statistically independent random variables $\mathbf{X}_j = \{X_j^m\}_{m=1}^M$ with expected values $\mathbf{A}_j \boldsymbol{\theta}_j$, the statistical model for the reconstructed TAC is written as:

$$\mathbf{x}_j = \mathbf{A}_j \boldsymbol{\theta}_j + \boldsymbol{\varepsilon}_j \quad (8)$$

where $\boldsymbol{\varepsilon}_j \in \mathbb{R}^{M \times 1}$ is a vector of normally distributed random noise with zero mean. The parameters can be estimated in any voxel by weighted least-square regression:

$$\widehat{\boldsymbol{\theta}_j} = \left(\mathbf{A}_j^T \mathbf{W} \mathbf{A}_j \right)^{-1} \mathbf{A}_j^T \mathbf{W} \mathbf{x}_j \quad (9)$$

where a hat denotes estimates of parameters and $\mathbf{W} \in \mathbb{R}^{M \times M}$ is a diagonal weighting matrix whose elements are inversely proportional to the variance of the PET measurements. The elements of the weighting matrix are often defined as the frame durations. In practice, the TAC in the reference region $\bar{\mathbf{x}}_R = [\bar{x}_R^1 \ldots \bar{x}_R^M]^T$ (1^{st} column of $\mathbf{A}_j$) is obtained by

averaging the activity measured in a cerebellum ROI. Note that Eq. (9) can estimate positive or negative values for γ, reflecting increases or decreases in neurotransmitter levels.

2.2.2. Proposed method: direct parametric reconstruction

The DPR method directly estimates the LSRRM parametric images from the measured dynamic projections. The key underlying assumption is that the coincidences detected during the scan represent noisy, Poisson-distributed projections of a four-dimensional (i.e. 3-D + time) activity distribution whose temporal attributes are governed by the kinetic model (LSRRM) and the unknown parametric maps to be estimated. In this work, estimation of the parametric images is performed by gradient-based optimization of a Poisson log-likelihood function that incorporates LSRRM kinetics and accounts for the effects of attenuation, head movement, detector sensitivity, randoms and scattered coincidences. Correction of head motion during DPR is performed by incorporating motion transformation matrices and frame-dependent attenuation coefficients inside the system matrix as explained hereinafter.

Data model. Let $\mathbf{y}^m = [y_1^m \ldots y_I^m]^T \in \mathbb{N}^{I\times 1}$ denote the vector of coincidences detected in the I lines of response (LORs) of the PET camera during an arbitrary frame m. We assume that the elements $\{y_i^m\}_{i=1}^I$ of $\mathbf{y}_m$ are statistically independent realizations of the random variables $\mathbf{Y}^m = \{Y_i^m\}_{i=1}^I$ having Poisson distributions with means $\bar{y}_i^m$ defined as

$$\bar{y}_i^m = \Delta_m \sum_{j=1}^{J} (\mathbf{P}_m)_{ij}\, \tilde{x}_j^m(\boldsymbol{\theta}_j) + \bar{s}_i^m + \bar{r}_i^m \tag{10}$$

where operator $(\ )_{ij}$ extracts the matrix entry at row i and column j, $\mathbf{P}_m \in \mathbb{R}^{I\times J}$ is the frame-dependent system matrix whose components are described afterwards, $\tilde{x}_j^m(\boldsymbol{\theta}_j)$ is the expected activity concentration value in voxel j that is determined by means of the kinetic model and parameters $\boldsymbol{\theta}_j$, $\bar{s}_i^m$ and $\bar{r}_i^m$ are the expected number of scattered and random coincidences, respectively, in LOR i and frame m. The factorized system matrix for a given frame is given by

$$\mathbf{P}_m = \mathbf{N}\mathbf{A}_m\mathbf{G}\mathbf{M}_{ref\to m} \tag{11}$$

where matrix $\mathbf{M}_{ref\to m} \in \mathbb{R}^{J\times J}$ is an operator that accounts for inter-frame head motion effects, transforming activity image $\{\tilde{x}_j^m(\boldsymbol{\theta}_j)\}_{j=1}^J$ from a reference head pose to the pose corresponding to frame m, $\mathbf{G} \in \mathbb{R}^{I\times J}$ is the geometric probability matrix with each element equal to the probability that a photon pair produced in voxel j is detected in LOR i in the absence of attenuation and sensitivity effects, $\mathbf{A}_m \in \mathbb{R}^{I\times I}$ is a diagonal matrix containing the attenuation coefficients in each LOR for frame m, and $\mathbf{N} \in \mathbb{R}^{I\times I}$ is a diagonal matrix that accounts LORs efficiencies and dead-time effects.

Parameter estimation. Let $\mathbf{y} = [\mathbf{y}^1, \ldots, \mathbf{y}^M]^T \in \mathbb{R}^{IM\times 1}$ denote the vector of coincidences measured in all the frames and $\boldsymbol{\theta} = [\boldsymbol{\theta}_1, \ldots, \boldsymbol{\theta}_J]^T \in \mathbb{R}^{4J\times 1}$ the unknown vector of parametric images. The Poisson likelihood density function for the projection data measured during the dynamic scan is

$$L(\mathbf{y};\boldsymbol{\theta}) = \prod_{m=1}^{M}\prod_{i=1}^{I} e^{-(\bar{y}_i^m)} \frac{(\bar{y}_i^m)^{y_i^m}}{y_i^m!} \tag{12}$$

The parametric maps are estimated by maximizing the log-likelihood function

$$\hat{\boldsymbol{\theta}} = \mathrm{argmax}_{\boldsymbol{\theta}} \log(L(\mathbf{y};\boldsymbol{\theta})) \tag{13}$$

where the expression for $\log(L(\mathbf{y};\boldsymbol{\theta}))$ is given by:

$$\log(L(\mathbf{y};\boldsymbol{\theta})) = \sum_{m=1}^{M}\sum_{i=1}^{I} -\left(\Delta_m \sum_{j=1}^{J} (\mathbf{P}_m)_{ij}\, \tilde{x}_j^m(\boldsymbol{\theta}_j) + \bar{s}_i^m + \bar{r}_i^m\right) + y_i^m \log\left(\Delta_m \sum_{j=1}^{J} (\mathbf{P}_m)_{ij}\, \tilde{x}_j^m(\boldsymbol{\theta}_j) + \bar{s}_i^m + \bar{r}_i^m\right) \tag{14}$$

The optimization problem in Eq. (13) was solved iteratively using a preconditioned conjugate gradient (PCG) algorithm described in the **Appendix**. The evaluation of the log-likelihood function in Eq. (14) during the optimization process involves the calculation of $\{\tilde{x}_j^m(\boldsymbol{\theta}_j)\}_{j,m}$, i.e., the dynamic distributions of activity synthesized by means of the current parameter estimates and LSRRM. Eq. (6) cannot be used in DPR to compute $\tilde{x}_j^m(\boldsymbol{\theta}_j)$ since the calculation of $\tilde{x}_j^m$ requires the knowledge of the time-integral of the same variable at this exact time point (see sums in the right-hand side of the equation). To compute $\tilde{x}_j^m(\boldsymbol{\theta}_j)$, we re-arrange Eq. (6) as:

$$\tilde{x}_j^m(\boldsymbol{\theta}_j) = \frac{R_1^j \bar{x}_R^m + k_2^j\left(\sum_{n=1}^{m}\frac{\Delta_n \bar{x}_R^n}{L_n} - \frac{\Delta_m \bar{x}_R^m}{2L_m}\right) - k_{2a}^j L_m \sum_{n=1}^{m-1}\frac{\Delta_n \tilde{x}_j^n(\boldsymbol{\theta}_j)}{L_n} - \gamma^j L_m \sum_{n=1}^{m-1}\frac{\Delta_n \tilde{x}_j^n(\boldsymbol{\theta}_j)}{L_n} h\left(t_n + \frac{\Delta_n}{2}\right)}{1 + k_{2a}^j\frac{\Delta_m}{2L_m} + \gamma^j\frac{\Delta_m}{2L_m} h\left(t_m + \frac{\Delta_m}{2}\right)}, \; m > 1$$

$$\tilde{x}_j^m(\boldsymbol{\theta}_j) = 0, \; m = 1 \tag{15}$$

The expression above indicates that, setting the initial condition $\tilde{x}_j^m(\boldsymbol{\theta}^j) = 0$ at $m = 1$, it is possible to recursively calculate $\tilde{x}_j^m(\boldsymbol{\theta}_j)$ at any frame based on the knowledge of its value at the preceding time frame, the parameter estimates, and the activity concentration history of the reference region. Note that both $\tilde{x}_j^m$ and $\bar{x}_R^m$ represent non-decay-corrected activity concentration measurements.

During the optimization, a positivity constraint is applied on activity values and on estimates of R_1, k_2 and k_{2a}. The positive constraint on parameters is implemented as follows: at each iteration, if $R_1^{j(n)}$, $k_2^{j(n)}$ or $k_{2a}^{j(n)} < \varepsilon$ (small positive value) and the PCG search direction ($\mathbf{a}^{(n)}$ in Eq. (1) of the **Appendix**) for the corresponding voxel and parameter is negative, the corresponding search direction value is set to zero. No constraint is applied on γ, which can be positive or negative.

ROI-targeted DPR. The projection model in Eq. (10) assumes that the kinetic model applies to any location in the field of view of the PET camera. However, this assumption may not hold true in practice, for example in voxels outside the brain such as in skull or mouth, which could in turn create modeling errors that may spatially propagate during DPR computation. The technique is thus modified to estimate kinetic parameters only in a pre-specified region of the image space within which time-varying activity concentrations are deemed to adhere closely to the underlying kinetic model. In order for the voxels located outside the ROI to still contribute to projections, the voxels located in the rest of the image space are assigned activity values obtained from a preliminary dynamic PET reconstruction. Specifically, the projection model is modified as

$$\bar{y}_i^m = \Delta_m \left(\sum_{j \in ROI} (\mathbf{P}_m)_{ij} \bar{x}_j^m(\boldsymbol{\theta}_j) + \sum_{j \notin ROI} (\mathbf{P}_m)_{ij} \hat{x}_j^m \right) + \bar{s}_i^m + \bar{r}_i^m \quad (16)$$

where $\hat{x}_j^m$ is the pre-calculated activity concentration in a voxel outside the chosen ROI. Data supporting the validity of this approach can be found in **Supplementary Material** (Supplemental Fig. 1).

Initialization. Because of the nonlinear relationship between the parametric images and the projection data, the log-likelihood in Eq. (14) is non-concave with respect to $\boldsymbol{\theta}$, and as a consequence, PCG can only guarantee convergence to a local optimum. Therefore, a judicious initial guess is critical for the algorithm to converge to an acceptable solution. Here, we initialized the PCG algorithm with the parametric maps obtained by applying IPR to smoothed dynamic PET images, under the assumption that the results obtained with IPR are in the same concave neighborhood as the "true" parametric images. Note also that initialization schemes based on smoothed results from the indirect method (as employed here) have been shown to make the convergence of DPR faster than with uniform parameter initialization, leading to lower bias in fewer iterations (Germino and Carson, 2018).

2.3. Simulation studies

We simulated ^{11}C-raclopride data mimicking an experimental protocol to evaluate the performance of the proposed methods. We used brain atlases included with the FSL software (http://fsl.fmrib.ox.ac.uk/fsl/fslwiki/) to create a 3-D numerical phantom (Fig. 1 A, voxel size = 2 × 2 × 2 mm^3) in the Montreal Neurological Institute (MNI) space, comprised of twenty-two different regions, including seven striatal functional subdivisions (Tziortzi et al., 2014). Results of SRTM analyses performed in sixteen subjects studied dynamically with ^{11}C-raclopride were used to assign realistic parameters values (R_1, k_2 and k_{2a}) to the voxels of each brain region. The human ^{11}C-raclopride data were also used to obtain a reference region TAC, calculated by averaging the cerebellum TACs across all subjects. These data where then used to generate three different sets of parametric images: two included ^{11}C-raclopride displacement in one sub-division of the striatum (executive area, as defined by (Tziortzi et al., 2014)) with magnitudes equal to $\gamma = 0.028$ min^{-1} and $\gamma = 0.014$ min^{-1}, respectively, and a third set had no displacement, i.e., $\gamma = 0$ min^{-1}. The selected displacement magnitudes corresponded to a peak receptor occupancy value of 40.1% and 23.6%, respectively. All simulations were performed using $h(t) = e^{-\alpha(t-t_s)}u(t-t_s)$ with $t_s = 27$ min and $\alpha = 0.22$ min^{-1} (Alpert et al., 2003). The parametric images and reference TAC were used to synthesize a noise-free TAC for each voxel using LSRRM (Eq. (15)), yielding activity images in 44 frames (10 × 30 s, 34 × 60 s), while accounting for radioactive decay of ^{11}C. Each activity volume of a specific frame was smoothed with a 3-D Gaussian filter (4.0 mm full width at half-maximum -FWHM) to mimic scanner's point spread function (PSF) effects, and was then forward-projected to a fully-3D

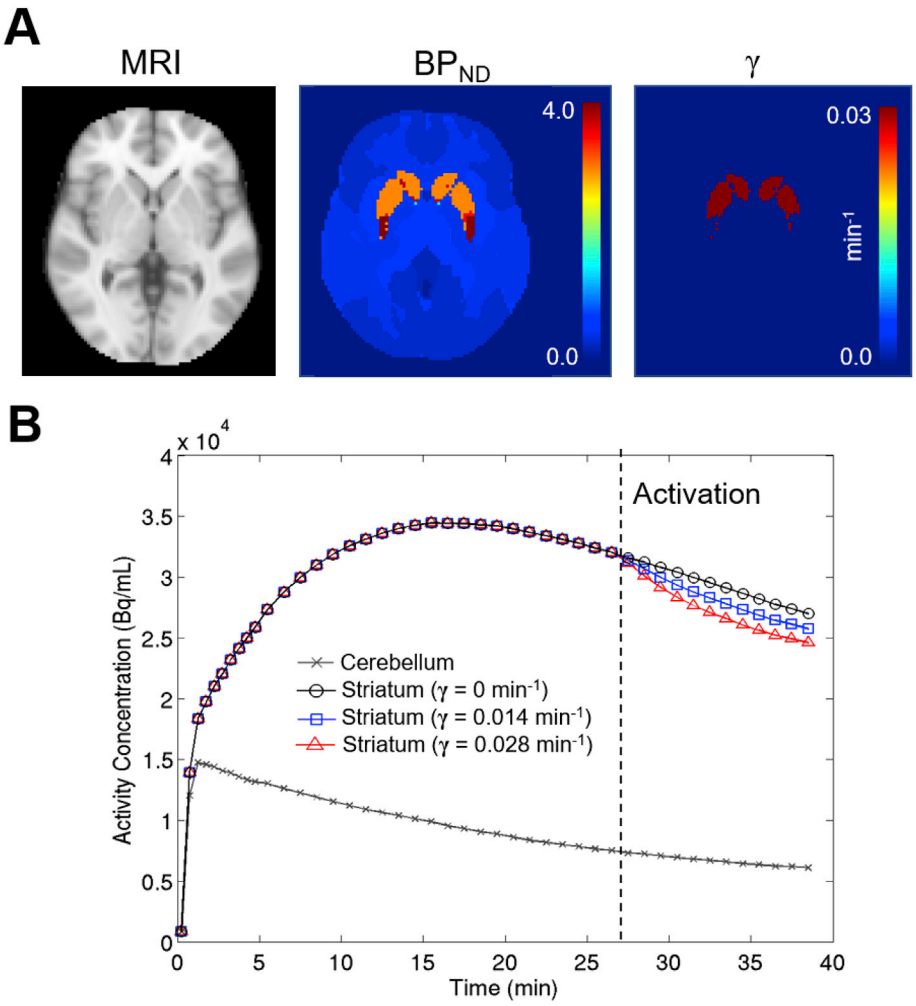

Fig. 1. Simulation of ^{11}C-raclopride data. **(A)** Brain phantom geometry with ground truth images of BP_{ND} and γ. The spatial distribution of $\gamma > 0$ corresponds to the executive area of the striatum (Tziortzi et al., 2014). **(B)** Examples of noise-free time-activity curves in the cerebellum (reference region, black crosses) and striatum (executive area) for different γ values.

sinogram with 344 distance bins, 252 angular bins and 837 projection planes (span = 11, maximum ring difference = 60), mimicking the geometry of the Biograph mMR PET/MR scanner (Siemens Healthineers, Erlangen, Germany). Next, the noise-free sinogram for each frame was multiplied with the sinogram of attenuation coefficients and LOR sensitivity. After scaling the dynamic sinograms to standard levels of detected true coincidences, Poisson deviates were applied to each sinogram bin to achieve noise levels comparable to our human studies (injection of ~13 mCi ^{11}C-raclopride). This resulted in a total number of ~380 million counts throughout the dynamic study. Thirty-two independent noise realizations were generated for each condition. Note that scattered and random coincidences were not simulated.

LSRRM parametric images were estimated using the standard and proposed method for each data set and noise realization. For the standard method, the sinogram for each frame was reconstructed using a fully-3D OSEM algorithm with standard corrections for attenuation and sensitivity. All images were reconstructed to a 128 × 128 × 127 matrix of 2 × 2 × 2 mm^3 pixels using 3 iterations and 21 subsets (standard reconstruction settings for the Biograph mMR scanner). Another set of images was obtained by applying a standard 4-mm FWHM Gaussian filter to each reconstructed volume. For each set of images, a TAC was extracted in the cerebellum (excluding the vermis) to serve as the reference TAC. Parametric images were then estimated by voxel-wise LSRRM fitting (Eq. (9)) of native ('IPR') and smoothed PET volumes ('IPR$_{smooth}$') using the corresponding reference TAC. For DPR, parametric images were estimated directly from the sinograms using Eq. (13) and the reference TAC extracted in native dynamic images. DPR computation was performed in a brain mask excluding the cerebellum.

Although there are four parameters in the LSRRM model, this report presents only the results for BP_{ND} and γ, the quantities of most interest in neurotransmission imaging. Images of bias, standard deviation (SD) and root mean square error (RMSE) across noise replicates were generated for BP_{ND} and γ according to:

$$\begin{aligned}
\mathrm{bias}\left(\hat{\theta}_j\right) &= \left\langle \hat{\theta}_j \right\rangle - \theta_j^{\mathrm{TRUE}} \\
\mathrm{SD}\left(\hat{\theta}_j\right) &= \sqrt{\frac{1}{N_r - 1}\sum_{n=1}^{N_r}\left(\hat{\theta}_{j,n} - \left\langle \hat{\theta}_j \right\rangle\right)^2} \\
\mathrm{RMSE}\left(\hat{\theta}_j\right) &= \sqrt{\frac{1}{N_r}\sum_{n=1}^{N_r}\left(\hat{\theta}_{j,n} - \theta_j^{\mathrm{TRUE}}\right)^2}
\end{aligned} \tag{17}$$

where $\langle \hat{\theta}_j \rangle = \frac{1}{N_r}\sum_{n=1}^{N_r}\hat{\theta}_{j,n}$ is the mean estimated parameter value across noise realizations in voxel j, N_r is the total number of replicates and θ_j^{TRUE} is the true parameter value. The calculation of bias, SD and RMSE involved rejection of outlier values, that is, parameter estimates with physiologically implausible values. For BP_{ND}, parameter estimates were arbitrarily considered as outliers if their value was less than zero or more than 3 times the maximum true BP_{ND} value in the striatum; accordingly, the range of 'accepted' values was set as $0 \leq BP_{ND} \leq 10$. For γ, negative values were kept and estimates were considered as outliers if their absolute value was more than 3 times higher than the true maximum value in striatum, resulting in a range of accepted values set as $-0.08 \leq \gamma \leq 0.08$ min^{-1}.

We also investigated whether DPR can help improve the detection of neurotransmitter release in a cohort of subjects. An "ideal" subject cohort (i.e., without inter-subject variability) was formed by considering the γ image estimated for a given noise realization as the measurement corresponding to one subject of the group. Detection of neurotransmitter release was then performed by applying a paired *t*-test (two-tailed), comparing stacked γ values against the null hypothesis (i.e., vector of zeros) on a voxel-by-voxel basis. This process was repeated for various numbers of "subjects" (N = 20, 15, 10 and 5) for IPR, IPR$_{smooth}$ and DPR data. No correction for multiple comparisons was performed. Images of the T-statistic were generated for each of the considered scenarios.

2.4. Human studies

Pilot ^{11}C-raclopride displacement studies were performed in two human subjects. Permission to conduct the study was obtained from the Massachusetts General Hospital Institutional Review Board and all subjects provided written informed consent. Subjects were scanned head first, supine on a hybrid PET/MR scanner (Biograph mMR, Siemens Healthineers) for 90-min in list mode following intravenous bolus injection of ~14 mCi of ^{11}C-raclopride. For each subject, a 3-D T1-weighted volume was acquired using a multi-echo MPRAGE sequence (Kouwe et al., 2008) with parameters: TR = 2530 ms, TEs = 1.69, 3.55, 5.41, 7.27 ms, flip angle = 7°, inversion time = 1100 ms, matrix size = 256 × 256 × 176 and voxel size = 1 × 1 × 1 mm^3. At about 27 min after tracer injection, a modified version of a monetary incentive delay (MID) task (Knutson et al., 2000, 2001) was started to induce striatal release of dopamine and ^{11}C-raclopride displacement while acquiring dynamic PET data. The MID task consisted of 150 trials presented over 25 min. Among these trials, ~75% were reward and ~25% were no-incentive trials. At each trial, a visual cue (1.5 s) signaling either potentially rewarding outcomes or no monetary incentive was presented on a monitor to the participant. After a fixed inter-stimulus-interval (2.0 s), participants pressed a button in response to a red square target, which was presented for 250 ms. A second inter-stimulus-interval (2.25s) followed the target, after which visual feedback (1.5 s) notified participants whether they won or not won money. Subjects were told that their reaction time to the target affected trial outcomes such that rapid reactions increased the probability of receiving gains and decreased the probability of receiving penalties.

The structural MRI scan of each subject was used to generate an attenuation map for PET using a previously validated hybrid segmentation-/atlas-based technique (Izquierdo-Garcia et al., 2014). The first 59-min of list-mode PET data were binned into 64 frames (10 × 30 s, 54 × 60 s). The sinogram data for each frame were then reconstructed and corrected for motion using the following multistep procedure. The first step was to obtain a frame-dependent attenuation map to ensure that emission and attenuation distributions were spatially consistent during reconstruction. To do so, we performed an initial reconstruction (OSEM, 3 iterations and 21 subsets) of the dynamic sinogram data without correction of attenuation, smoothed the resulting images with a Gaussian filter (6-mm FWHM) and used FSL's rigid-body registration with a normalized mutual information data consistency metric (Jenkinson and Smith, 2001) to align each frame to a selected reference frame (arbitrarily chosen as frame #20 of the dynamic scan, acquired 10 min after tracer injection). The normalized mutual information consistency metric was chosen over other criteria (e.g. least squares) because of its ability to handle data with varying intensity distributions such as dynamic PET images. The attenuation map was then registered to the resulting time-averaged volume and transformed using the previously calculated registration parameters, yielding an attenuation map for each dynamic frame. The second step performed another dynamic reconstruction, taking the frame-dependent attenuation map for attenuation correction of each frame. Note that the attenuation map also accounted for "non-moving" attenuating medium such as the scanner's bed and MRI head coil. The third and final step involved the registration of each frame to the reference frame, followed by a final registration of the dynamic images to the resulting time-averaged volume. The overall effectiveness of this procedure was verified by reviewing the dynamic images before and after motion correction. We also inspected selected TACs (that of the cerebellum in particular) and did not observe any abrupt change in the temporal evolution of the concentration that would suggest presence of residual motion effects after motion correction. The motion

transformation matrices for each frame were kept for incorporation within DPR (operator $\{\mathbf{M}_{ref\to m}\}_{m=1}^{M}$ in Eq. (11)). All reconstructions were performed on a $128 \times 128 \times 127$ matrix of $2 \times 2 \times 2$ mm^3 pixels using 3 iterations and 21 subsets, as per usual iteration settings on the mMR. LSRRM parametric images were then estimated using IPR (voxel-wise fitting -Eq. 9- of native dynamic images), IPR_{smooth} (voxel-wise fitting of dynamic images smoothed with a standard 4-mm FWHM Gaussian filter) and DPR (Eq. (13)). The reference region TAC used during kinetic modeling was derived using a cerebellum mask obtained after elastic registration of the MNI T1-weigthed MR atlas to each subject's MPRAGE volume using FSL. For DPR, parameter estimation was performed within a brain mask (defined with MRI) that excluded the cerebellum. All methods employed an activation function defined as: $h(t) = e^{-\alpha(t-t_s)}u(t-t_s)$ (Alpert et al., 2003) with t_s set as the start time of the task. The value of α, which controls the rate at which activation effects dissipates after task onset, was set as $\alpha = 0.05$ min^{-1} (half-life: 13.9 min), ensuring that the perturbation period covered the duration of the MID task. Note that other displacement studies with a reward task have set α to a similar value (Ceccarini et al., 2012). The maps produced for larger values of α ($\alpha = 0.1$ and 0.2 min^{-1}) can be found in **Supplemental Material** (Supplemental Fig. 4 and 5).

2.5. Data and code availability statement

The code and data used in this work will be made available upon reasonable request and may not be used for commercial purposes.

3. Results

Fig. 2 shows the evolution of the bias versus standard deviation (SD) trade off (panel A) and the RMSE (panel B) in striatum for BP_{ND} and γ as a function of the number of iterations. The curves in panel A indicate that the DPR method offers a more favorable bias-SD trade off than the conventional approaches: for example, DPR yields lower BP_{ND} bias than IPR_{smooth} at matched SD level, and conversely, it achieves lower SD than IPR_{smooth} at matched levels of BP_{ND} bias. DPR estimates of γ have lower bias and SD than those obtained with IPR and IPR_{smooth}. The BP_{ND} bias seen for all methods for a large number of iterations can be explained by the PET point spread function, whose effects were modeled during data generation. As expected, BP_{ND} bias is more substantial for IPR_{smooth} due to the application of a Gaussian filter prior to LSRRM fitting. As can be seen in Fig. 2 B, for a relatively small number of PCG iterations (<~30), DPR estimates of BP_{ND} are characterized by a noticeably lower RMSE compared with IPR and IPR_{smooth}. The RMSE associated to DPR

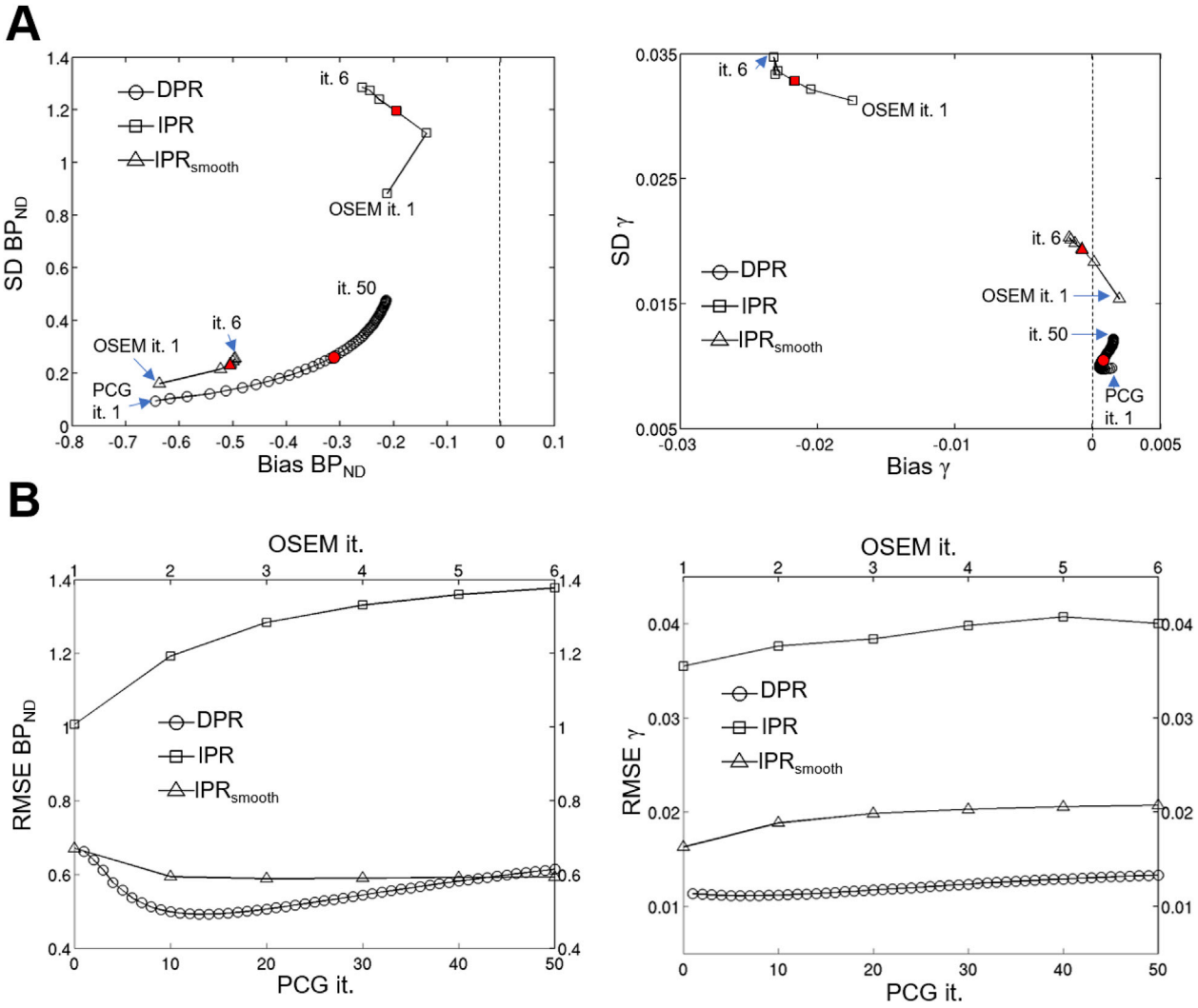

Fig. 2. Evolution of (**A**) bias versus standard deviation (SD) trade off and (**B**) root-mean-square error (RMSE) in striatum (executive area, $BP_{ND}^{TRUE} = 3.0$ and $\gamma^{TRUE} = 0.028$ min^{-1}) as a function of iteration number. Results for BP_{ND} and γ are shown in the left and right columns, respectively. Iteration numbers for DPR and IPR/IPR_{smooth} respectively correspond to the number of PCG updates and OSEM iterations. The red filled symbols in **(A)** mark the number of OSEM and PCG iterations used for IPR/IPR_{smooth} and DPR, respectively, in the rest of the study.

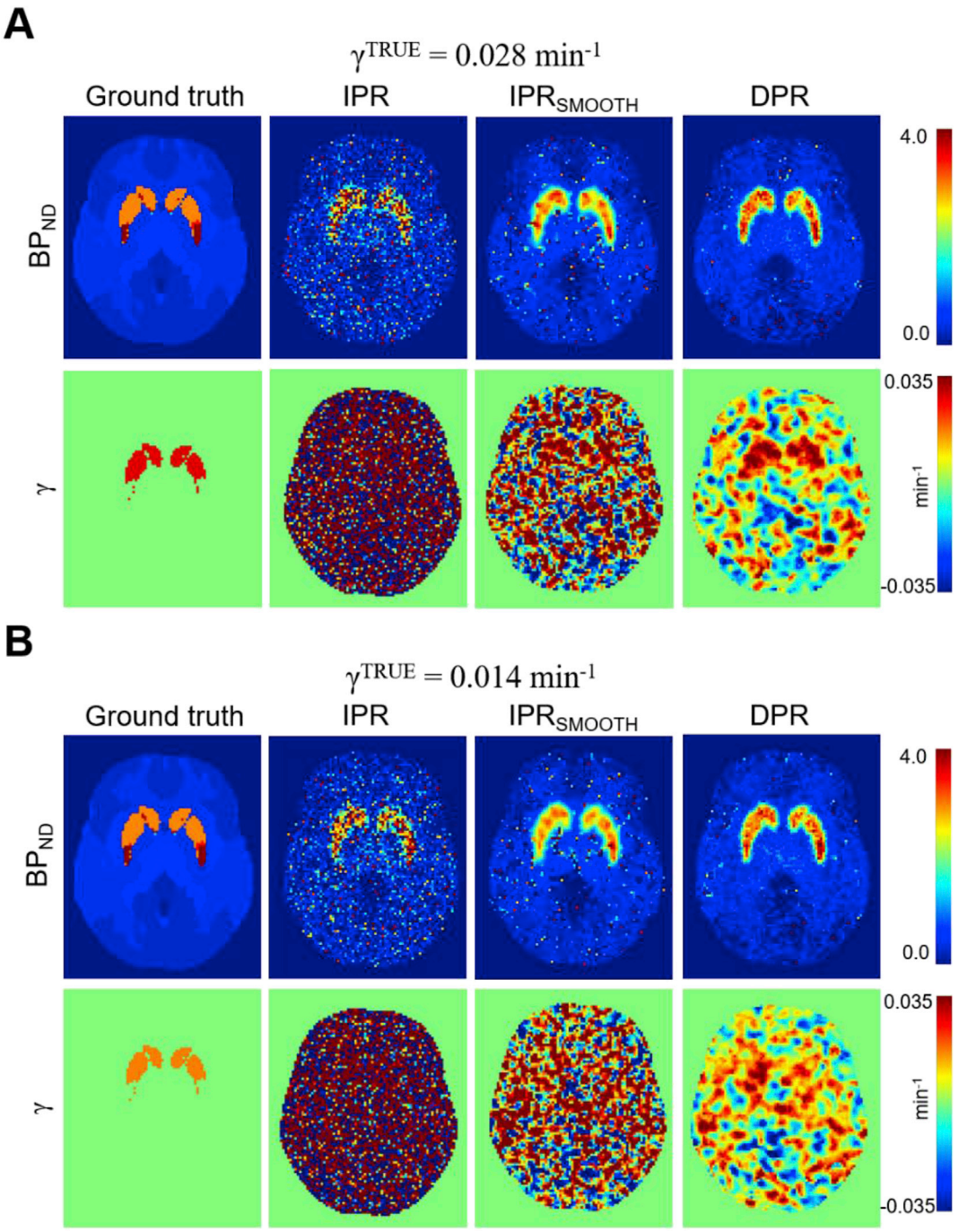

Fig. 3. Representative examples of BP_{ND} and γ images computed using conventional and proposed approaches for two levels of displacement: (**A**) $\gamma^{TRUE} = 0.028$ min^{-1} and (**B**) $\gamma^{TRUE} = 0.014$ min^{-1}. Ground truth images are shown in the left-most column of each panel. DPR was performed using 16 PCG iterations; IPR/IPR$_{smooth}$ was performed using OSEM with 3 iterations, 21 subsets.

quantification of γ is likewise substantially smaller than that of conventional approaches.

Note that the DPR results presented thereafter were generated using 16 PCG updates, which corresponds to the number of iterations yielding the lowest BP_{ND} RMSE in striatum (see Fig. 2 B). The iteration yielding the lowest RMSE was chosen as the stopping criterion for DPR as it provides a good tradeoff between accuracy and prevision, with a bias level close to the value in the converged regime and a relatively low noise level. The IPR/IPR$_{smooth}$ results were obtained using activity images reconstructed with the standard OSEM iteration settings for the mMR scanner (i.e., 3 iterations, 21 subsets). As can be seen on Fig. 2 B, this number of OSEM iterations also corresponds to a point where striatal BP_{ND} RMSE is nearly minimal for IPR$_{smooth}$; therefore, the comparison between DPR and IPR$_{smooth}$ in the rest of the study is performed for iteration levels minimizing the RMSE for each approach.

Fig. 3 shows representative examples of BP_{ND} and γ images obtained for two displacement magnitudes: $\gamma^{TRUE} = 0.028$ min^{-1} (panel A) and $\gamma^{TRUE} = 0.014$ min^{-1} (panel B). Ground truth parametric images are shown in the left-most column of each panel. By visual inspection, γ images estimated using DPR exhibit clearly higher SNR than those obtained with IPR and IPR$_{smooth}$, despite residual false-positive activations outside the striatum. DPR likewise provides low-noise BP_{ND} maps with fewer outliers compared with other approaches, especially in low-binding, extrastriatal areas. It is also interesting to note that DPR yields

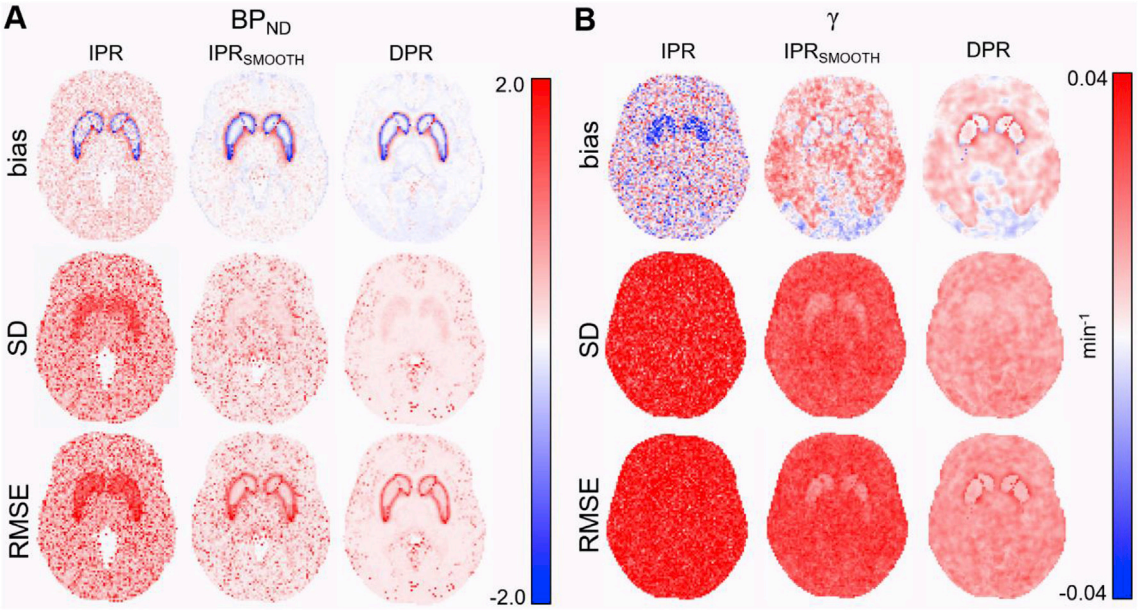

Fig. 4. Comparison of bias (top row), standard deviation ('SD', middle row) and root-mean square error ('RMSE', bottom row) for (**A**) BP_{ND} and (**B**) γ, using the different approaches. The simulated release magnitude was $\gamma^{TRUE} = 0.028$ min^{-1}.

Table 1
Bias, standard deviation (SD), root-mean-square error (RMSE), mean value and percentage of outliers for BP_{ND} and γ in a striatum ROI for the various simulation setups and estimation approaches. True BP_{ND} value in the ROI: 3.0; true values for γ are reported in the table.

	$\gamma^{TRUE} = 0.028$ min^{-1}			$\gamma^{TRUE} = 0.014$ min^{-1}			$\gamma^{TRUE} = 0.0$ min^{-1}		
	IPR	IPR$_{smooth}$	DPR	IPR	IPR$_{smooth}$	DPR	IPR	IPR$_{smooth}$	DPR
Mean BP_{ND}	2.82	2.51	2.69	2.79	2.50	2.69	2.69	2.51	2.69
Bias BP_{ND}	−0.18	−0.49	−0.31	−0.21	−0.50	−0.31	−0.31	−0.49	−0.31
SD BP_{ND}	1.26	0.24	0.27	1.25	0.24	0.26	1.27	0.26	0.27
RMSE BP_{ND}	1.32	0.59	0.49	1.32	0.60	0.50	0.49	0.59	0.50
% outliers BP_{ND}	17.3	0.02	0.0	18.0	0.0	0.0	17.8	0.01	0.0
Mean γ	0.006	0.027	0.029	0.004	0.010	0.017	0.003	0.007	0.006
Bias γ	−0.022	−0.0007	0.0005	−0.010	0.004	0.003	0.003	0.007	0.006
SD γ	0.033	0.019	0.010	0.033	0.021	0.010	0.033	0.023	0.010
RMSE γ	0.039	0.020	0.011	0.035	0.022	0.011	0.034	0.024	0.012
% outliers γ	68.7	14.4	0.57	66.6	5.5	0.0	65.5	2.3	0.0

Table 2
Bias, standard deviation (SD), root-mean-square error (RMSE), mean value and percentage of outliers for BP_{ND} and γ in a representative gray matter ROI for the various simulation setups and estimation approaches. True BP_{ND} value in the ROI: 0.43; true γ value: 0.0 min^{-1} (no release was simulated outside the striatum).

	$\gamma^{TRUE} = 0.028$ min^{-1}			$\gamma^{TRUE} = 0.014$ min^{-1}			$\gamma^{TRUE} = 0.0$ min^{-1}		
	IPR	IPR$_{smooth}$	DPR	IPR	IPR$_{smooth}$	DPR	IPR	IPR$_{smooth}$	DPR
Mean BP_{ND}	0.62	0.45	0.41	0.62	0.47	0.42	0.64	0.46	0.43
Bias BP_{ND}	0.19	0.02	−0.01	0.19	0.04	−0.01	0.21	0.033	−0.001
SD BP_{ND}	0.66	0.31	0.16	0.67	0.37	0.17	0.69	0.35	0.18
RMSE BP_{ND}	0.68	0.32	0.17	0.69	0.37	0.18	0.72	0.35	0.18
% outliers BP_{ND}	23.4	7.0	0.24	23.4	7.0	0.39	24.5	8.30	0.29
Mean γ	-.0001	0.014	0.008	0.001	0.014	0.008	0.002	0.014	0.009
Bias γ	-.0001	0.014	0.008	0.001	0.014	0.008	0.002	0.014	0.009
SD γ	0.034	0.026	0.013	0.033	0.025	0.014	0.033	0.026	0.014
RMSE γ	0.034	0.029	0.015	0.034	0.029	0.016	0.033	0.029	0.016
% outliers γ	71.1	12.5	0.02	69.9	12.9	0.03	70.2	12.3	0.04

higher BP_{ND} values than IPR$_{smooth}$ in the striatum, which can be explained by the absence of spatial smoothing in the direct estimation framework. Note that images of all LSRRM parameters (R_1, k_2, k_{2a} and γ) computed using the various methods are included in Supplemental Fig. 2.

Fig. 4 displays maps of bias, SD and RMSE for BP_{ND} and γ over all noise realizations for simulated displacement magnitude: $\gamma^{TRUE} = 0.028$ min^{-1}. Tables 1 and 2 present average bias, SD and RMSE values as well as percentage of outliers in a striatal and gray matter ROI, respectively, for the various displacement strengths. Raw histograms of BP_{ND} and γ in the striatal and gray matter ROIs can be found in Supplemental Fig. 3. DPR estimates of γ in the striatal ROI have low bias and significantly smaller SD than conventional approaches, leading up to 1.8- and 3.5-fold reduction in γ RMSE as compared to IPR$_{smooth}$ and IPR, respectively. The SD of striatal BP_{ND} estimation by DPR is much lower (~4.8-fold) than

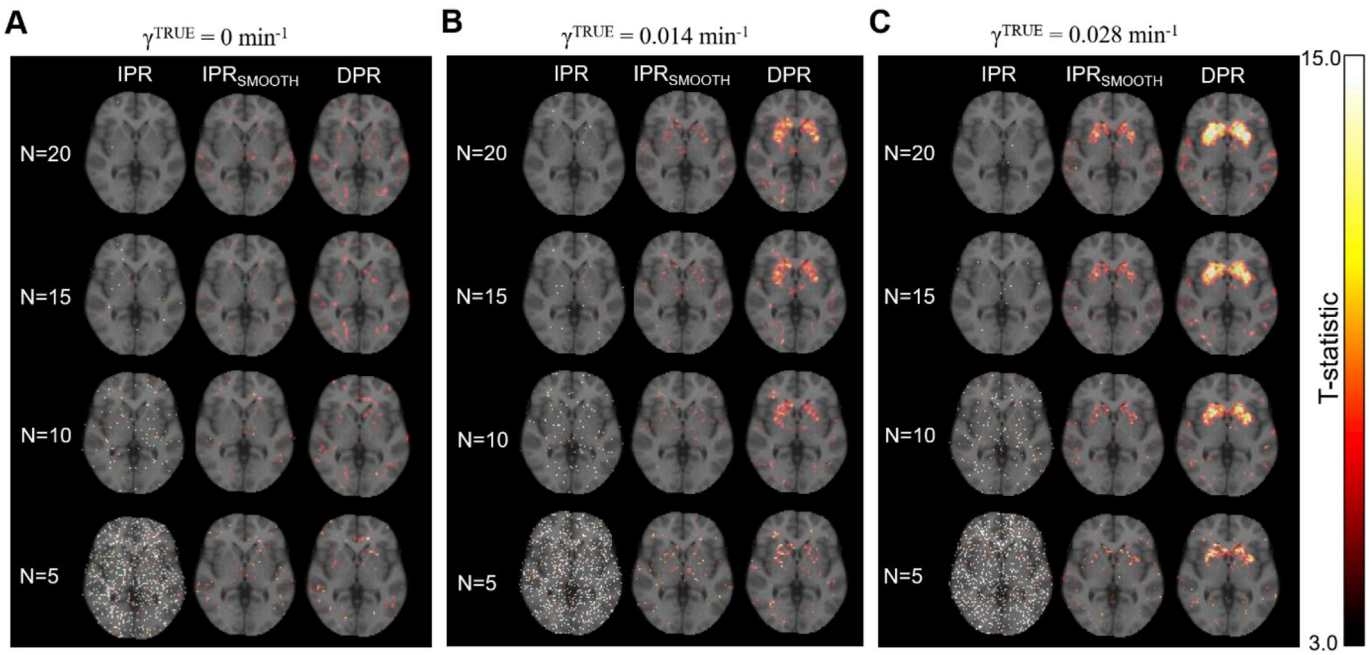

Fig. 5. T-statistic for varying numbers of "subjects" (N = 20, 15, 10 or 5) and displacement magnitudes: (A) $\gamma^{TRUE} = 0.0$ min^{-1}, (B) $\gamma^{TRUE} = 0.014$ min^{-1} and (C) $\gamma^{TRUE} = 0.028$ min^{-1}. Results are overlaid on T1w MRI to facilitate visual inspection. IPR detects no release even for N = 20 and $\gamma^{TRUE} = 0.028$ min^{-1}. DPR clearly outperforms both IPR and IPR$_{smooth}$ approaches and can detect release even with N = 5 or $\gamma^{TRUE} = 0.014$ min^{-1}.

that of IPR, but equivalent to that achieved using IPR$_{smooth}$. Nevertheless, due to Gaussian smoothing, IPR$_{smooth}$ is associated with high BP$_{ND}$ bias whereas the bias of DPR remains small. Consequently, the RMSE of DPR BP$_{ND}$ quantification is substantially lower than that of IPR$_{smooth}$. DPR estimation of BP$_{ND}$ and γ produced few outliers, with levels lower than 1% in both striatal and cortical ROIs. The number of outliers for IPR$_{smooth}$ in striatum was also small for BP$_{ND}$ but higher for γ, ranging between 2 and ~15% depending on the magnitude of the simulated displacement. IPR estimation was very unstable, with levels of outliers exceeding 65% for γ and 17% for BP$_{ND}$ in striatum and cortex. Note also that the negative BP$_{ND}$ bias observable for all methods at the edges of the striatum (see Fig. 4 A) may be attributed to the effects of the PSF. For DPR, the use of smoothed parametric images for initialization of the method may also contribute to this bias.

Results analyzing the effect of DPR on the detectability of neurotransmitter release are presented in Fig. 5. Each panel in the figure shows maps of the T-statistic (overlaid on structural MRI), testing whether the null hypothesis ($\gamma \leq 0$, i.e. no release) can be rejected in a given voxel. A given row in each panel corresponds to a different number of "subjects" (N = 20, 15, 10 or 5). Panel A presents the data for no simulated release ($\gamma^{TRUE} = 0.0$ min^{-1}) whereas results in panels B and C respectively correspond to a weak ($\gamma^{TRUE} = 0.014$ min^{-1}) and more substantial ($\gamma^{TRUE} = 0.028$ min^{-1}) release. Panels B and C show that with IPR, release cannot be reliably detected even with N = 20 and $\gamma^{TRUE} = 0.028$ min^{-1}. IPR$_{smooth}$ allows for detection of displacement under certain conditions, e.g. $\gamma^{TRUE} = 0.028$ min^{-1} and N $\geq$ 10 or for $\gamma^{TRUE} = 0.14$ min^{-1} and N $\geq$ 20. As can be seen, the DPR technique drastically improves release detectability and can detect an effect even for N = 5 and $\gamma^{TRUE} = 0.028$ min^{-1} or for N = 10 and $\gamma^{TRUE} = 0.014$ min^{-1}, whereas the standard methods clearly cannot.

Fig. 6 displays representative examples of BP$_{ND}$ and γ images obtained for the two human data sets. The white dashed line overlaid on γ maps delineates the striatum to facilitate visual inspection of these results. DPR estimates of γ images exhibit lower pixel-wise variability than those obtained with conventional methods. Visual inspection of γ images obtained with all approaches reveal areas of elevated signal in the putamen of both subjects that might suggest potential displacement of ^{11}C-raclopride. In agreement with observations made with simulations, DPR yielded BP$_{ND}$ maps exhibiting fewer outliers, and markedly higher values in the putamen and caudate nucleus compared to IPR$_{smooth}$. Fig. 7 presents examples of TACs extracted in "activated" voxels of the putamen in both subjects along with model fits obtained from the different estimators (IPR, IPR$_{smooth}$, DPR). Changes in the TACs can be observed following the initiation of the MID task, suggesting potential ^{11}C-raclopride displacement.

As can be seen in Fig. 6, all approaches estimated large γ values outside the striatum, especially in areas exhibiting very low BP$_{ND}$. The results of extrastriatal γ quantification should however be interpreted with caution for two reasons: one, because estimates of γ in low binding regions have a large variance and error, as underscored by the simulation results; and two, because quantification of ^{11}C-raclopride data using cerebellum as the reference region is in general not adapted for surveying dopamine signaling in extrastriatal regions (Svensson et al., 2019; Dagher and Palomero-Gallagher, 2020; Backes, 2020).

4. Discussion

Receptor ligand-based PET scanning has been used for many years to detect and quantify transient changes in endogenous neurotransmitter concentration in response to pharmacologic and cognitive stimulation. The analysis of dynamic scan data measured during a single-scan neuromodulation study typically follows a two-step process consisting in reconstructing the projection measurements into a temporal sequence of PET images first, followed by least-square fitting of estimated TACs to a non-steady state pharmacokinetic model such as LSRRM. However, due to the high statistical fluctuations in PET concentration data of single voxels, parameter estimation is very unstable at the voxel level and parametric images obtained using this approach have notoriously low SNR. The high noise level not only reduces the accuracy and precision of voxel-wise neurotransmitter release quantification at the subject level, it also reduces the overall statistical power of this imaging methodology, which makes it in turn necessary to use large sample sizes for testing neuroscientific hypotheses in cohorts.

In this work, we have presented a DPR computational framework that estimates 3-D distributions of LSRRM parameters, including binding potential (BP$_{ND}$) and neurotransmitter release magnitude (γ), directly

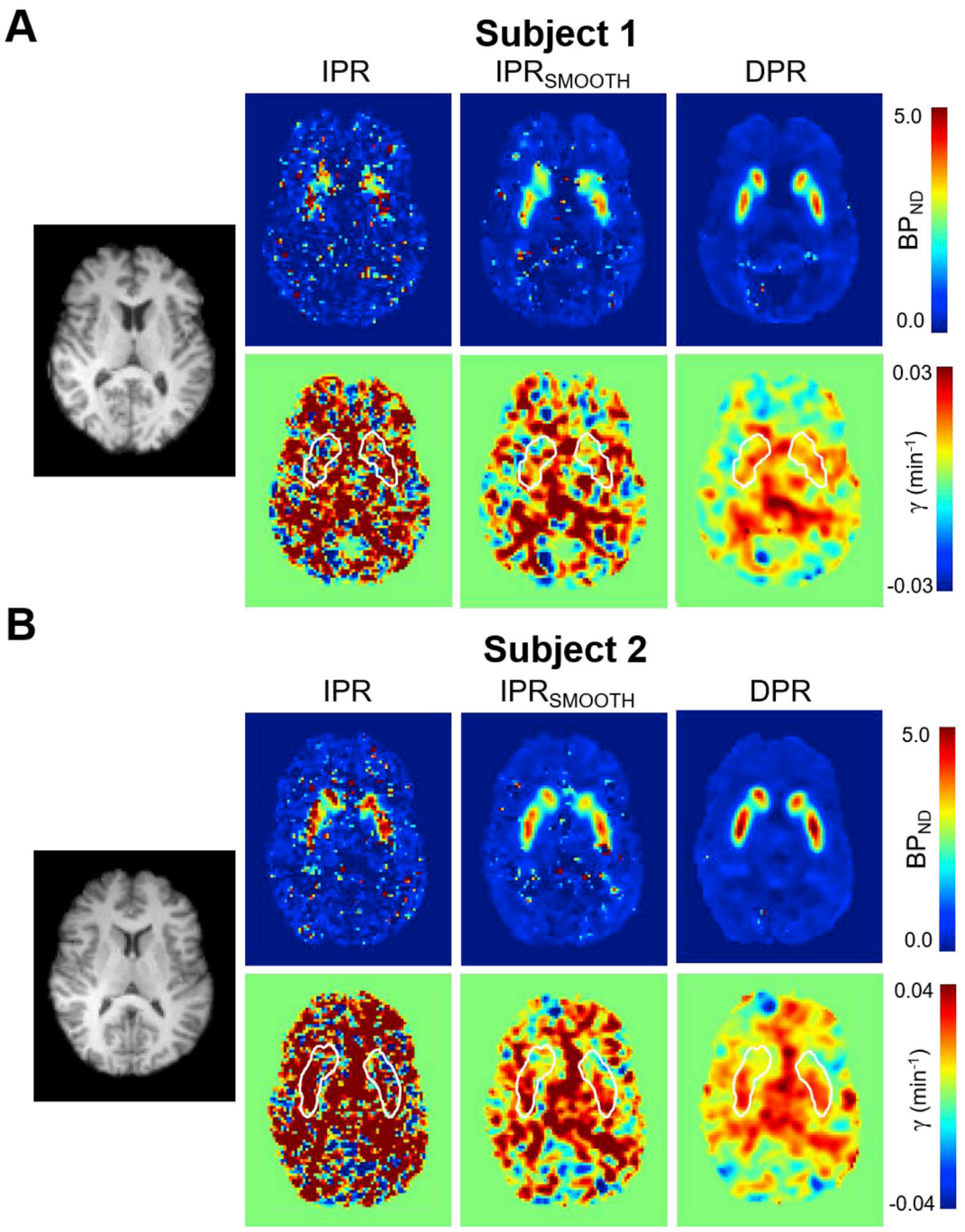

Fig. 6. Representative images of BP_{ND} and γ obtained using the different methods for the two human subjects with $\alpha = 0.05\ min^{-1}$. The white dashed line overlaid on γ maps delineates the striatum to facilitate visual inspection of the results. DPR was performed using 16 PCG iterations; IPR/IPR_{smooth} was performed using OSEM with 3 iterations, 21 subsets.

from dynamic projection data and evaluated its performance against that of standard approaches using simulated and human ^{11}C-raclopride experiments. Our simulation findings showed that the proposed approach significantly improves the accuracy and precision of voxel-wise LSRRM parameter estimation, yielding images of BP_{ND} and γ with a substantially improved SNR. Furthermore, we showed that detection of neurotransmitter release could be made more reliable and/or conducted with smaller sample sizes by using the proposed DPR estimator. The applicability of the proposed methodology for human investigation was demonstrated in two subjects studied with ^{11}C-raclopride and a monetary reward task used to induce dopamine release and tracer displacement. As with any novel *in vivo* displacement study, the ground truth is unknown; it is thus not possible to know whether dopamine release did occur, and there is no attempt to draw conclusions about brain networks or activation foci in this study. Instead, the evaluation focused on comparing the quality of the LSRRM parametric images obtained with the different approaches, the purpose being to demonstrate that changes in actual human studies are similar to those observed in simulations. In many aspects, the improvement observed in human ^{11}C-raclopride studies closely matched that observed in simulations, with estimated images of BP_{ND} and γ exhibiting lower noise and higher SNR than those obtained with conventional approaches. To our knowledge, this is one of the first studies investigating the use of direct parametric reconstruction for imaging neuromodulatory changes in human subjects.

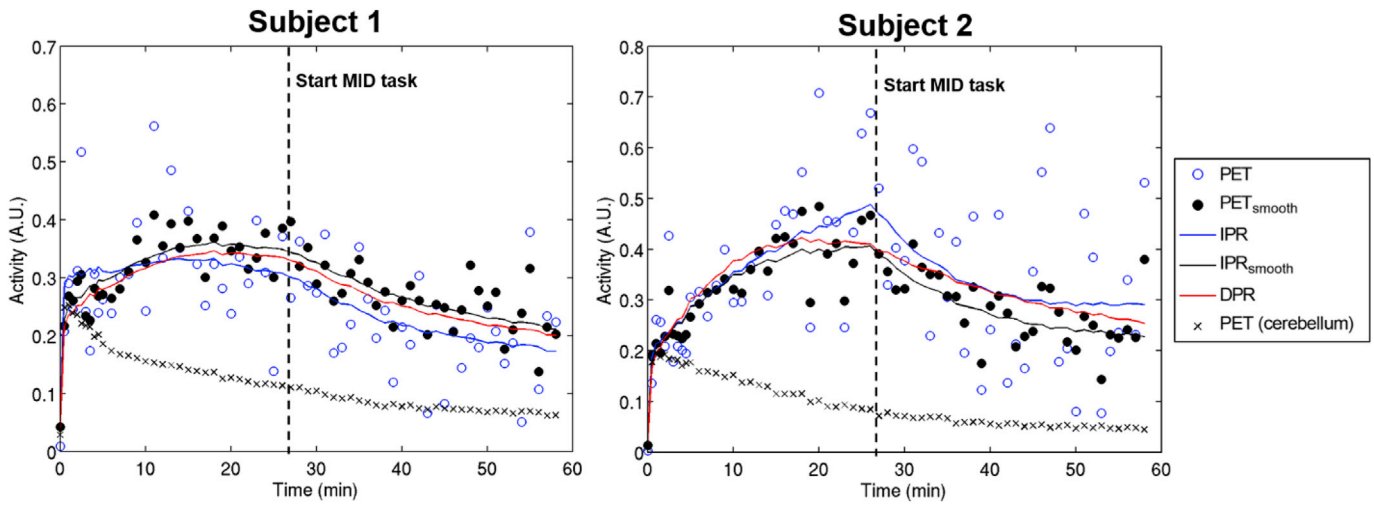

Fig. 7. Examples of time activity curves and model fits in the two subjects. For each subject, the empty (resp. filled) circle symbols indicate the PET activity extracted in native (resp. smoothed) OSEM volumes in an "activated" putamen voxel. The cross symbols indicate PET activity from the cerebellum reference region. The solid lines represent LSRRM fits obtained using IPR, IPR_{smooth} and DPR with $\alpha = 0.05$ min^{-1}. The vertical line at t ~27 min denotes the start time of the task.

The parametric images estimated by DPR were compared to those obtained by least-square fitting of native and smoothed images obtained with a standard iterative PET reconstruction algorithm. Overall, LSRRM fitting of native PET volumes (the 'IPR' method) yielded poor results, producing voxel-wise estimates of BP_{ND} and γ with very low accuracy and precision and a large number of outliers. As a result, as shown in Fig. 5, this method could not detect displacement in any of the considered scenarios, including for a displacement of a large magnitude in an "ideal" cohort of 20 subjects. Apart from the low SNR of TACs for single voxels, two other factors may explain the poor performance of this parameter estimation approach. First, the independent variable of the regression (matrix $\mathbf{A_j}$, Eq. (7)) is not noise-free since some of its components (e.g. 3rd and 4th columns) are computed by temporal integration of noisy activity concentration data, which violates the fundamental principles of ordinary least-square estimation. Second, due to the structure of the kinetic model, variables $\mathbf{x_j}$ and $\mathbf{A_j}$ are not independent, which makes noise in the two variables correlated and can introduce bias in parameter estimates (R. E. Carson, 1993; Ichise et al., 2002, 2003). Spatial filtering of PET images with a Gaussian kernel prior to LSRRM fitting (the 'IPR_{smooth}' method) significantly improved the precision of parameter estimation, yielding γ distributions that allowed for statistical detection of neurotransmitter release in some of the considered scenarios (Fig. 5). Smoothing reduces noise in PET activity concentration data; consequently, the variance of parameter estimates is lower for IPR_{smooth} than for IPR based on properties of least-square estimation. In addition, smoothing may improve the conditioning of least-square fitting problem compared to IPR, since the corresponding independent variables ($\mathbf{A_j}$ matrices) are formed using data exhibiting lower noise. However, smoothing resulted in a decrease in the resolution of imaging data and increased bias, which can be well appreciated by inspecting BP_{ND} quantification in the striatum.

By contrast, the proposed DPR method retained the spatial resolution of the original data due to the absence of spatial smoothing operations. As a result, it produced BP_{ND} estimates in striatum with a much lower bias compared to IPR_{smooth}. Overall, the accuracy and precision of DPR parameter estimates was higher than that of standard methods. As can be seen in Fig. 5, the method also led to drastic reduction in type-II errors, enabling statistical detection of a moderate displacement with as little as 5 "subjects" whereas the standard methods clearly could not. Nevertheless, visual inspection of Figs. 3 and 5 also shows that DPR did not fully eliminate type I errors (false positives) outside the striatum. Incorporation of spatial regularization in the DPR framework (e.g. through a Bayesian prior) is expected to drastically alleviate such errors, albeit at the expense of increased bias. It can also be noted that in general, the SNR improvement afforded by DPR depended on the local noise level in the image. Comparison of BP_{ND} estimation results in striatum versus cortex (Tables 1 and 2) indicate that areas of lower SNR such as the cortex benefited the most from DPR, whereas there were more modest improvements in precision for the striatum.

DPR performed generally better than IPR and IPR_{smooth} for three main reasons. First, the DPR estimator is more statistically efficient than the indirect ones because better estimates of noise are available for PET projection data (Poisson) than are for reconstructed activity concentration histories. Second, DPR essentially introduces temporal regularization into the reconstruction of dynamic emission data via the LSRRM kinetic model, whereas the indirect methods do not. Third, DPR circumvents the aforementioned limitations of least-square parameter estimation associated to indirect approaches.

In the current implementation, the DPR estimator relies on several sources of information extracted from preliminary estimations of activity and kinetic parameters conducted using traditional approaches. First, the algorithm utilizes a cerebellum TAC derived from an initial dynamic PET reconstruction to compute activity concentration values from parameters at each iteration (Eq. (15)). Second, the system matrix (Eq. (11)) of the DPR forward model incorporates two pre-calculated components: the inter-frame motion transformations and the frame-dependent attenuation correction coefficients. Here, motion transformation operators were determined by applying rigid-body registration to non-attenuation corrected dynamic images, and the frame-dependent attenuation map was obtained by applying these transformations to the acquired MR-based attenuation map. Note that, while this has not been explored in the current work, some investigators have proposed to jointly perform estimation of head motion and parametric images directly from dynamic projection measurements (Jiao et al., 2017). Third, the initialization of the PCG algorithm was performed using parametric images obtained by pixel-wise fitting of smoothed PET images. The DPR method is indeed sensitive to initialization owing to the nonlinear relationship between the log-likelihood function and the parameters, and a judicious initial guess is critical to ensure that the algorithm converges towards a low-bias solution. Finally, time-varying activity concentration values - determined using an initial dynamic reconstruction - were assigned to all voxels located outside the region chosen for application of DPR so that these voxels could also contribute to projections during parametric image reconstruction.

The LSRRM analysis technique was originally developed to detect stimulus-induced changes in neurotransmitter concentration for single-

scan PET neurotransmission experiments. The key feature of LSRRM is its use of a time-varying apparent radioligand clearance rate parameter ($k_{2a}(t)$ in Eq. (1)) that incorporates the effect of neurotransmitter release on the PET curve. A limitation of the method, however, is its use of a canonical function (exponential with known onset and decay times, see Eq. (3)) to describe the shape of the neurotransmission response profile. In practice, this limits the application of LSRRM to stimuli that elicit responses whose onsets coincide with the time of stimulus initiation, are instantaneously maximal and decline at a fixed rate. To address these shortcomings, Normandin and colleagues (Normandin et al., 2012) developed lp-ntPET, a basis-function extension of LSRRM designed to detect and characterize neurotransmitter responses that may have greater complexity than the exponential function prescribed in LSRRM. Responses in lp-ntPET are represented by gamma variate basis functions (Madsen, 1992) whose parameters are identified from the function that best fits the activity concentration histories. Importantly, the timing of the onset of the activation pattern needs not be known a priori with lp-ntPET. Owing to the basis function implementation of the model, DPR of lp-ntPET parametric maps would be most efficiently implemented using algorithms that optimize the four-dimensional log-likelihood function (Eq. (14)) by decoupling the dynamic reconstruction and voxel-wise kinetic fitting processes (e.g. (Matthews et al., 2010; Wang and Qi, 2009, 2008)), rather than by gradient-based optimization as employed in this work. In their recent publication, Angelis et al., (2018) extended Matthew's approach (Matthews et al., 2010) to implement direct estimation of lp-ntPET parameters for application in imaging of awake rats.

The methodology employed to simulate ^{11}C-raclopride activity concentration data was not ideal. Indeed, by using LSRRM to generate noise-free TACs instead of the full neurotransmitter PET model (Morris et al., 2005), we have neglected the potential effects of modeling errors which can spatially propagate during DPR (Kotasidis et al., 2011). Furthermore, in the human study, we set α, the rate of decline in activation effect, to a nominal value ($\alpha = 0.05\ \text{min}^{-1}$). Although this has not been explored in the present work, it would be in principle possible to estimate a subject- and/or region-specific α and to recompute the parametric maps using the estimated values.

One of the main drawbacks of DPR is the computational burden of the estimation as the calculation of the log-likelihood and its gradient requires projection and back-projection operations that map the entire dynamic sequence of images to the fully-3D sinogram domain and vice-versa. For the current implementation of the DPR method, one iteration of PCG takes ~7 min on our computer cluster of 32 nodes, each of which equipped with a 2-processor 8-core Intel Xeon 2.4 GHz CPU. The computational load of DPR could be significantly reduced by implementing the forward and back-projectors either on GPUs or with an optimized multi-threaded CPU implementation.

5. Conclusion

In this study, we presented and evaluated a computational framework that directly estimates 3-D images of LSRRM parameters from dynamic projections measured during a single-scan PET neuromodulation experiment. Analyses of realistically simulated ^{11}C-raclopride data demonstrated that the proposed approach drastically increases the SNR of the estimated parametric maps, improving the characterization of neurotransmitter release magnitude and ligand binding potential as compared to standard estimators. Detectability of neurotransmitter release improved with the proposed method, allowing detection of weaker effects and reducing the needed sample size. Application of the method in human subjects was demonstrated using ^{11}C-raclopride data and a reward task, confirming the improved quality of the estimated parametric images compared to traditional approaches.

Declaration of competing interest

Over the past three years, D.A.P has received consulting fees from Akili Interactive Labs, BlackThorn Therapeutics, Boehringer Ingelheim, and Takeda and an honorarium from Alkernes, for activities unrelated to the current paper. No funding from these entities was used to support the current work, and all views expressed are solely those of the authors. All other authors report no biomedical financial interests.

Acknowledgments

This work was supported in part by grants P41-EB022544 (YP, NMA, JO, GEF, MDN), R21-MH121812 (YP, MDN, JO), R01-MH100350 (MDN, NMA, GEF, DAP) and R01-MH102279 (MF, CC, DAP) from the National Institutes of Health (NIH). DAP was partially supported by NIH grant R37-MH068376. The content is solely the responsibility of the authors and does not necessarily represent the official views of the NIH. The funding organization had no role in the design and conduct of the study; collection, management, analysis, and interpretation of the data; preparation, review, or approval of the manuscript; and decision to submit the manuscript for publication.

Appendix A. Supplementary data

Supplementary data to this article can be found online at https://doi.org/10.1016/j.neuroimage.2020.117154.

APPENDIX. Preconditioned conjugate gradient algorithm

The optimization problem in Eq. (13) is solved iteratively using a preconditioned conjugate gradient (PCG) algorithm:

$$\begin{aligned}
\boldsymbol{\theta}^{(n+1)} &= \boldsymbol{\theta}^{(n)} + \alpha^{(n)}\mathbf{a}^{(n)} \\
\mathbf{a}^{(n)} &= \mathbf{d}^{(n)} + \beta^{(n-1)}\mathbf{a}^{(n-1)} \\
\mathbf{d}^{(n)} &= \mathbf{Q}^{(n)}\mathbf{g}^{(n)} \\
\beta^{(n-1)} &= \frac{\left(\mathbf{g}^{(n)} - \mathbf{g}^{(n-1)}\right)^{T}\mathbf{d}^{(n)}}{\left(\mathbf{g}^{(n-1)}\right)^{T}\mathbf{d}^{(n-1)}}
\end{aligned} \tag{1}$$

Where n is the PCG iteration number, $\mathbf{g}^{(n)} \in \mathbb{R}^{4J\times 1}$ is the gradient vector of the log-likelihood function at $\boldsymbol{\theta} = \boldsymbol{\theta}^{(n)}$ and $\mathbf{a}^{(n)} \in \mathbb{R}^{4J\times 1}$ is the PCG search vector initialized with $\mathbf{a}^{(0)} = \mathbf{d}^{(0)}$. Scalar $\alpha^{(n)}$ in Eq. (1) is the step-size, which is determined using Armijo's line-search method (Armijo, 1966). Matrix

$\mathbf{Q}^{(n)} = \mathrm{diag}(q_j^{l(n)}) \in \mathbb{R}^{4J\times 4J}$ is the preconditioner matrix whose entries are given by (Rakvongthai et al., 2013; Petibon et al., 2017):

$$q_j^{l(n)} = \frac{\left|\theta_j^{l(n)}\right|}{\overline{S}_j \left|\sum_{m=1}^{M} \frac{\partial \bar{x}_j^m(\boldsymbol{\theta}_j)}{\partial \theta_j^l}\right|_{\boldsymbol{\theta}_j=\boldsymbol{\theta}_j^{(n)}}} \tag{2}$$

where $l = 1\ldots4$ indexes the model parameters and $\overline{S}_j$ is a sensitivity term defined as

$$\overline{S}_j = \sum_{m=1}^{M} f_m \sum_{i=1}^{I} (\mathbf{P}_m)_{ij} \tag{3}$$

with $f_m = \Delta_m / \sum_{m=1}^{M} \Delta_m$.

References

Abi-Dargham, A., Gil, R., Krystal, J., Baldwin, R.M., Seibyl, J.P., Bowers, M., van Dyck, C.H., Charney, D.S., Innis, R.B., Laruelle, M., 1998. Increased striatal dopamine transmission in schizophrenia: confirmation in a second cohort. Am. J. Psychiatr. 155 (6), 761–767. https://doi.org/10.1176/ajp.155.6.761.

Alpert, Nathaniel M., Badgaiyan, Rajendra D., Livni, Elijahu, Fischman, Alan J., 2003. A novel method for noninvasive detection of neuromodulatory changes in specific neurotransmitter systems. Neuroimage 19 (3), 1049–1060. https://doi.org/10.1016/S1053-8119(03)00186-1.

Angelis, G.I., Gillam, J.E., Ryder, W.J., Fulton, R.R., Meikle, S.R., 2018. Direct estimation of voxel-wise neurotransmitter response maps from dynamic PET data. IEEE Trans. Med. Imag. https://doi.org/10.1109/TMI.2018.2883756, 1–1.

Armijo, Larry, 1966. Minimization of functions having lipschitz continuous first partial derivatives. Pac. J. Math. 16 (1), 1–3. https://doi.org/10.2140/pjm.1966.16.1.

Backes, Heiko, 2020. [11C]Raclopride and extrastriatal binding to D2/3 receptors. Neuroimage 207 (February), 116346. https://doi.org/10.1016/j.neuroimage.2019.116346.

Barrett, H.H., Wilson, D.W., Tsui, B.M.W., 1994. Noise properties of the EM algorithm. I. Theory. Phys. Med. Biol. 39 (5), 833. https://doi.org/10.1088/0031-9155/39/5/004.

Breier, A., Su, T.-P., Saunders, R., Carson, R.E., Kolachana, B.S., de Bartolomeis, A., Weinberger, D.R., et al., 1997. "Schizophrenia is associated with elevated amphetamine-induced synaptic dopamine concentrations: evidence from a novel Positron emission Tomography Method. Proc. Natl. Acad. Sci. U.S.A. 94 (6), 2569–2574.

Busto, Usoa E., Redden, Laura, Mayberg, Helen, Kapur, Shitij, Sylvain Houle, Laurie, A., Zawertailo, 2009. Dopaminergic activity in depressed smokers: a Positron emission Tomography study. Synapse 63 (8), 681–689. https://doi.org/10.1002/syn.20646.

Carson, R.E., 1993. PET Parameter Estimation Using Linear Integration Methods : Bias and Variability Considerations, 1993. https://ci.nii.ac.jp/naid/10025135725/.

Carson, Richard E., Breier, Alan, de Bartolomeis, Andrea, Saunders, Richard C., Su, Tom P., Schmall, Bernard, Margaret, G. Der, Pickar, David, Eckelman, William C., 1997. Quantification of amphetamine-induced changes in [11C]raclopride binding with continuous infusion , quantification of amphetamine-induced changes in [11C] raclopride binding with continuous infusion. J. Cerebr. Blood Flow Metabol. 17 (4), 437–447. https://doi.org/10.1097/00004647-199704000-00009.

Carson, Richard E., Lange, Kenneth, 1985. Comment: the EM parametric image reconstruction algorithm. J. Am. Stat. Assoc. 80 (389), 20–22. https://doi.org/10.1080/01621459.1985.10477120.

Ceccarini, J., Vrieze, E., Koole, M., Muylle, T., Bormans, G., Claes, S., Van Laere, K., 2012. Optimized in vivo detection of dopamine release using 18F-fallypride PET. J. Nucl. Med. 53 (10), 1565–1572. https://doi.org/10.2967/jnumed.111.099416.

Constantinescu, C.C., Bouman, C., Morris, E.D., 2007. Nonparametric extraction of transient changes in neurotransmitter concentration from dynamic PET data. IEEE Trans. Med. Imag. 26 (3), 359–373. https://doi.org/10.1109/TMI.2006.891501.

Cox, Sylvia M.L., Benkelfat, Chawki, Dagher, Alain, Scott Delaney, J., Durand, France, McKenzie, Samuel A., Kolivakis, Theodore, Casey, Kevin F., Leyton, Marco, 2009. Striatal dopamine responses to intranasal cocaine self-administration in humans. Biol. Psychiatr. 65 (10), 846–850. https://doi.org/10.1016/j.biopsych.2009.01.021.

Dagher, Alain, Palomero-Gallagher, Nicola, 2020. Mapping dopamine with Positron emission Tomography: a note of caution. Neuroimage 207 (February), 116203. https://doi.org/10.1016/j.neuroimage.2019.116203.

Endres, C.J., Carson, R.E., 1998. Assessment of dynamic neurotransmitter changes with bolus or infusion delivery of neuroreceptor ligands. J. Cerebr. Blood Flow Metabol. 18 (11), 1196–1210. https://doi.org/10.1097/00004647-199811000-00006. Official Journal of the International Society of Cerebral Blood Flow and Metabolism.

Fessler, J.A., 1996. Mean and variance of implicitly defined biased estimators (such as penalized maximum likelihood): applications to Tomography. IEEE Trans. Image Process. 5 (3), 493–506. https://doi.org/10.1109/83.491322.

Friston, Karl J., Malizia, Andrea L., Wilson, Susan, Cunningham, Vincent J., Jones, Terry, Nutt, David J., 1997. "Analysis of dynamic radioligand displacement or 'activation' studies. J. Cerebr. Blood Flow Metabol. 17 (1), 80–93. https://doi.org/10.1097/00004647-199701000-00011.

Fuente-Fernández, Raúl de la, Ruth, Thomas J., Sossi, Vesna, Schulzer, Michael, Calne, Donald B., Jon Stoessl, A., 2001. Expectation and dopamine release: mechanism of the placebo effect in Parkinson's disease. Science 293 (5532), 1164–1166. https://doi.org/10.1126/science.1060937.

Germino, Mary, Carson, Richard E., 2018. Cardiac-gated parametric images from ^{82}Rb PET from dynamic frames and direct 4D reconstruction. Med. Phys. 45 (2), 639–654. https://doi.org/10.1002/mp.12710.

Gravel, Paul, Reader, Andrew J., 2015. Direct 4D PET MLEM reconstruction of parametric images using the simplified reference tissue model with the basis function method for [11C] raclopride. Phys. Med. Biol. 60 (11), 4533.

Ichise, Masanori, Jeih-San Liow, Lu, Jian-Qiang, Takano, Akihiro, Model, Kendra, Toyama, Hiroshi, Suhara, Tetsuya, Suzuki, Kazutoshi, Innis, Robert B., Carson, Richard E., 2003. Linearized reference tissue parametric imaging methods: application to [11C] DASB Positron emission Tomography studies of the serotonin transporter in human brain. J. Cerebr. Blood Flow Metabol. 23 (9), 1096–1112.

Ichise, Masanori, Toyama, Hiroshi, Innis, Robert B., Carson, Richard E., 2002. Strategies to improve neuroreceptor parameter estimation by linear regression analysis. J. Cerebr. Blood Flow Metabol. 22 (10), 1271–1281. https://doi.org/10.1097/01.WCB.0000038000.34930.4E. Official Journal of the International Society of Cerebral Blood Flow and Metabolism.

Izquierdo-Garcia, David, Hansen, Adam E., Förster, Stefan, Benoit, Didier, Schachoff, Sylvia, Fürst, Sebastian, Chen, Kevin T., Chonde, Daniel B., Catana, Ciprian, 2014. An SPM8-based approach for attenuation correction combining segmentation and nonrigid template formation: application to simultaneous PET/MR brain imaging. J. Nucl. Med. 55 (11), 1825–1830. https://doi.org/10.2967/jnumed.113.136341.

Jenkinson, Mark, Smith, Stephen, 2001. A global optimisation method for robust affine registration of brain images. Med. Image Anal. 5 (2), 143–156. https://doi.org/10.1016/S1361-8415(01)00036-6.

Jiao, J., Bousse, A., Thielemans, K., Burgos, N., Weston, P.S.J., Schott, J.M., Atkinson, D., et al., 2017. Direct parametric reconstruction with joint motion estimation/correction for dynamic brain PET data. IEEE Trans. Med. Imag. 36 (1), 203–213. https://doi.org/10.1109/TMI.2016.2594150.

Kamasak, M.E., Bouman, C.A., Morris, E.D., Sauer, K., 2005. Direct reconstruction of kinetic parameter images from dynamic PET data. IEEE Trans. Med. Imag. 24 (5), 636–650. https://doi.org/10.1109/TMI.2005.845317.

Knutson, Brian, Fong, Grace W., Adams, Charles M., Varner, Jerald L., Hommer, Daniel, 2001. Dissociation of reward anticipation and outcome with event-related FMRI. Neuroreport 12 (17), 3683.

Knutson, Brian, Westdorp, Andrew, Kaiser, Erica, Hommer, Daniel, 2000. FMRI visualization of brain activity during a monetary incentive delay task. Neuroimage 12 (1), 20–27. https://doi.org/10.1006/nimg.2000.0593.

Koepp, M.J., Gunn, R.N., Lawrence, A.D., Cunningham, V.J., Dagher, A., Jones, T., Brooks, D.J., Bench, C.J., Grasby, P.M., 1998. Evidence for striatal dopamine release during a video game. Nature 393 (6682), 266–268. https://doi.org/10.1038/30498.

Kotasidis, Fotis A., Matthews, Julian C., I Angelis, Georgios, Markiewicz, Pawel J., Lionheart, William R., Reader, Andrew J., 2011. Impact of erroneous kinetic model formulation in direct 4D image reconstruction. In: Nuclear Science Symposium and Medical Imaging Conference (NSS/MIC), 2011 IEEE. IEEE, pp. 2366–2367. https://doi.org/10.1109/NSSMIC.2011.6153881.

Kouwe, André J. W. van der, Thomas Benner, Salat, David H., Fischl, Bruce, 2008. Brain morphometry with multiecho MPRAGE. Neuroimage 40 (2), 559–569. https://doi.org/10.1016/j.neuroimage.2007.12.025.

Lammertsma, Adriaan A., Hume, Susan P., 1996. Simplified reference tissue model for PET receptor studies. Neuroimage 4 (3), 153–158. https://doi.org/10.1006/nimg.1996.0066.

Lidstone, Sarah C., Schulzer, Michael, Dinelle, Katherine, Mak, Edwin, Sossi, Vesna, Ruth, Thomas J., de la Fuente-Fernández, Raul, Phillips, Anthony G., Jon Stoessl, A., 2010. Effects of expectation on placebo-induced dopamine release in Parkinson disease. Arch. Gen. Psychiatr. 67 (8), 857–865. https://doi.org/10.1001/archgenpsychiatry.2010.88.

Lippert, Rachel N., Cremer, Anna Lena, Thanarajah, Sharmili Edwin, Korn, Clio, Jahans-Price, Thomas, Burgeno, Lauren M., Tittgemeyer, Marc, Brüning, Jens C., Walton, Mark E., Backes, Heiko, 2019. Time-dependent assessment of stimulus-evoked regional dopamine release. Nat. Commun. 10 (1) https://doi.org/10.1038/s41467-018-08143-4.

Madsen, M.T., 1992. A simplified formulation of the gamma variate function. Phys. Med. Biol. 37 (7), 1597–1600. https://doi.org/10.1088/0031-9155/37/7/010.

Martinez, Diana, Gil, Roberto, Slifstein, Mark, Hwang, Dah-Ren, Huang, Yiyun, Perez, Audrey, Lawrence, Kegeles, et al., 2005. Alcohol dependence is associated with blunted dopamine transmission in the ventral striatum. Biol. Psychiatr. 58 (10), 779–786. https://doi.org/10.1016/j.biopsych.2005.04.044.

Matthews, J.C., Angelis, G.I., Kotasidis, F.A., Markiewicz, P.J., Reader, A.J., 2010. Direct reconstruction of parametric images using any spatiotemporal 4D image based model and maximum likelihood expectation maximisation. In: IEEE Nuclear Science Symposuim Medical Imaging Conference. https://doi.org/10.1109/NSSMIC.2010.5874225, 2435–41.

Morris, Evan D., Yoder, Karmen K., Wang, Chunzhi, Normandin, Marc D., Zheng, Qi-Huang, Mock, Bruce, Raymond, F. Muzic, Froehlich, Janice C., 2005. NtPET: a new application of PET imaging for characterizing the kinetics of endogenous neurotransmitter release. Mol. Imag. 4 (4), 7290. https://doi.org/10.2310/7290.2005.05130, 2005.05130.

Normandin, Marc D., Schiffer, Wynne K., Morris, Evan D., 2012. A linear model for estimation of neurotransmitter response profiles from dynamic PET data. Neuroimage 59 (3), 2689–2699. https://doi.org/10.1016/j.neuroimage.2011.07.002.

Pappata, S., Dehaene, S., Poline, J.B., Gregoire, M.C., Jobert, A., Delforge, J., Frouin, V., et al., 2002. In vivo detection of striatal dopamine release during reward: a PET study with [11C]raclopride and a single dynamic scan approach. Neuroimage 16 (4), 1015–1027. https://doi.org/10.1006/nimg.2002.1121.

Petibon, Yoann, Rakvongthai, Yothin, El Fakhri, Georges, Ouyang, Jinsong, 2017. Direct parametric reconstruction in dynamic PET myocardial perfusion imaging: in vivo studies. Phys. Med. Biol. 62 (9), 3539. https://doi.org/10.1088/1361-6560/aa6394.

Rahmim, Arman, Tang, Jing, Zaidi, Habib, 2009. Four-dimensional (4D) image reconstruction strategies in dynamic PET: beyond conventional independent frame reconstruction. Med. Phys. 36 (8), 3654–3670.

Rakvongthai, Yothin, Ouyang, Jinsong, Guerin, Bastien, Li, Quanzheng, Nathaniel, M Alpert, El Fakhri, Georges, 2013. Direct reconstruction of cardiac PET kinetic parametric images using a preconditioned conjugate gradient approach. Med. Phys. 40 (10), 102501.

Reader, Andrew J., Verhaeghe, Jeroen, 2014. 4D image reconstruction for emission Tomography. Phys. Med. Biol. 59 (22), R371.

Singer, Harvey S., Szymanski, Sally, Giuliano, Joseph, Yokoi, Fuji, Dogan, A. Semih, Brasic, James R., Zhou, Yun, Grace, Anthony A., Wong, Dean F., 2002. "Elevated intrasynaptic dopamine release in Tourette's syndrome measured by PET. Am. J. Psychiatr. 159 (8), 1329–1336. https://doi.org/10.1176/appi.ajp.159.8.1329.

Snyder, D.L., 1984. Parameter estimation for dynamic studies in emission-tomography systems having list-mode data. IEEE Trans. Nucl. Sci. 31 (2), 925–931. https://doi.org/10.1109/TNS.1984.4333400.

Steeves, T.D.L., Miyasaki, J., Zurowski, M., Lang, A.E., Pellecchia, G., Van Eimeren, T., Rusjan, P., Houle, S., Strafella, A.P., 2009. Increased striatal dopamine release in parkinsonian patients with pathological gambling: a [11C] raclopride PET study. Brain 132 (5), 1376–1385. https://doi.org/10.1093/brain/awp054.

Svensson, Jonas E., Martin, Schain, Pontus, Plavén-Sigray, Simon, Cervenka, Mikael, Tiger, Magdalena, Nord, Christer, Halldin, Lars, Farde, Johan, Lundberg, 2019. Validity and reliability of extrastriatal [11C]raclopride binding quantification in the living human brain. Neuroimage 202 (November), 116143. https://doi.org/10.1016/j.neuroimage.2019.116143.

Tedroff, J., Pedersen, M., Aquilonius, S.M., Hartvig, P., Jacobsson, G., Långström, B., 1996. "Levodopa-Induced changes in synaptic dopamine in patients with Parkinson's disease as measured by [11C]raclopride displacement and PET. Neurology 46 (5), 1430–1436.

Tsoumpas, Charalampos, Turkheimer, Federico E., Thielemans, Kris, 2008. A survey of approaches for direct parametric image reconstruction in emission Tomography. Med. Phys. 35 (9), 3963–3971.

Tziortzi, Andri C., Haber, Suzanne N., Searle, Graham E., Tsoumpas, Charalampos, Long, Christopher J., Paul, Shotbolt, Douaud, Gwenaelle, et al., 2014. Connectivity-based functional analysis of dopamine release in the striatum using diffusion-weighted MRI and Positron emission Tomography. Cerebr. Cortex 24 (5), 1165–1177. https://doi.org/10.1093/cercor/bhs397.

Volkow, N.D., Wang, G.-J., Fowler, J.S., Logan, J., Gatley, S.J., Hitzemann, R., Chen, A.D., Dewey, S.L., Pappas, N., 1997. Decreased striatal dopaminergic responsiveness in detoxified cocaine-dependent subjects. Nature 386 (6627), 830–833. https://doi.org/10.1038/386830a0.

Wang, Qi, 2008. Iterative nonlinear least squares algorithms for direct reconstruction of parametric images from dynamic PET. In: 2008 5th IEEE International Symposium on Biomedical Imaging: from Nano to Macro. https://doi.org/10.1109/ISBI.2008.4541175, 1031–34.

Wang, Guobao, Qi, Jinyi, 2009. Generalized algorithms for direct reconstruction of parametric images from dynamic PET data. IEEE Trans. Med. Imag. 28 (11), 1717–1726.

Wang, Guobao, Qi, Jinyi, 2010. Acceleration of the direct reconstruction of linear parametric images using nested algorithms. Phys. Med. Biol. 55 (5), 1505–1517. https://doi.org/10.1088/0031-9155/55/5/016.

Wang, Guobao, Qi, Jinyi, 2013. Direct estimation of kinetic parametric images for dynamic PET. Theranostics 3 (10), 802–815.

Wong, Dean F., Brašić, James R., Singer, Harvey S., Schretlen, David J., Kuwabara, Hiroto, Zhou, Yun, Nandi, Ayon, et al., 2008. Mechanisms of dopaminergic and serotonergic neurotransmission in tourette syndrome: clues from an in vivo neurochemistry study with PET. Neuropsychopharmacology 33 (6), 1239–1251. https://doi.org/10.1038/sj.npp.1301528. Official Publication of the American College of Neuropsychopharmacology.

Yan, Jianhua, Planeta-Wilson, Beata, Carson, Richard E., 2012. Direct 4-D PET list mode parametric reconstruction with a novel EM algorithm. IEEE Trans. Med. Imag. 31 (12), 2213–2223.